

Key Points:

- Antarctic shelf sediments underlying marginal sea ice cover exhibit high sedimentation and remineralization rates of organic carbon
- A high degree of sedimentary Fe-recycling is found which scales with organic carbon remineralization rates
- Coupling between P and Fe recycling is observed with a constant P/Fe flux ratio of 0.26 for sediments with high Fe and P recycling rates

Correspondence to:

M. Baloza,
marwa.baloza@awi.de

Citation:

Baloza, M., Henkel, S., Geibert, W., Kasten, S., & Holtappels, M. (2022). Benthic carbon remineralization and iron cycling in relation to sea ice cover along the eastern continental shelf of the Antarctic Peninsula. *Journal of Geophysical Research: Oceans*, 127, e2021JC018401. <https://doi.org/10.1029/2021JC018401>



Received 8 JAN 2022

Accepted 16 JUN 2022

© 2022. The Authors.

This is an open access article under the terms of the [Creative Commons Attribution License](#), which permits use, distribution and reproduction in any medium, provided the original work is properly cited.

Benthic Carbon Remineralization and Iron Cycling in Relation to Sea Ice Cover Along the Eastern Continental Shelf of the Antarctic Peninsula

M. Baloza^{1,2} , S. Henkel¹ , W. Geibert¹ , S. Kasten^{1,3}, and M. Holtappels^{1,4} 

¹Alfred Wegener Institute Helmholtz Centre for Polar and Marine Research, Bremerhaven, Germany, ²Faculty 2 Biology / Chemistry, University Bremen, Bremen, Germany, ³Faculty of Geosciences, University Bremen, Bremen, Germany, ⁴MARUM - Center for Marine Environmental Sciences, University of Bremen, Bremen, Germany

Abstract Rapid and profound climatic and environmental changes have been predicted for the Antarctic Peninsula with so far unknown impact on the biogeochemistry of the continental shelves. In this study, we investigate benthic carbon sedimentation, remineralization and iron cycling using sediment cores retrieved on a 400 mile transect with contrasting sea ice conditions along the eastern shelf of the Antarctic Peninsula. Sediments at comparable water depths of 330–450 m showed sedimentation and remineralization rates of organic carbon, ranging from 2.5 to 13 and 1.8–7.2 mmol C m⁻² d⁻¹, respectively. Both rates were positively correlated with the occurrence of marginal sea ice conditions (5%–35% ice cover) along the transect, suggesting a favorable influence of the corresponding light regime and water column stratification on algae growth and sedimentation rates. From south to north, the burial efficiency of organic carbon decreased from 58% to 27%, while bottom water temperatures increased from –1.9 to –0.1°C. Net iron reduction rates, as estimated from pore-water profiles of dissolved iron, were significantly correlated with carbon degradation rates and contributed 0.7%–1.2% to the total organic carbon remineralization. Tightly coupled phosphate-iron recycling was indicated by significant covariation of dissolved iron and phosphate concentrations, which almost consistently exhibited P/Fe flux ratios of 0.26. Iron efflux into bottom waters of 0.6–4.5 μmol Fe m⁻² d⁻¹ was estimated from an empirical model. Despite the deep shelf waters, a clear benthic-pelagic coupling is indicated, shaped by the extent and duration of marginal sea ice conditions during summer, and likely to be affected by future climate change.

Plain Language Summary The seafloor of the shallow shelf seas plays a significant role in the recycling of organic carbon and acts as a nutrient source for algae growth in the upper water layers. In Antarctic waters, the change in sea ice cover has a great impact on the growth of algae and the subsequent sinking of organic carbon to the seafloor. With global warming, profound changes in sea ice cover are expected for the Antarctic Peninsula. To better understand its imprint on the seafloor, we collected sediment samples from different locations along the eastern shelf of the Antarctic Peninsula and measured how changes in sea ice cover influence the accumulation and recycling of organic carbon. We found that moderate sea ice cover of 5%–35% increases the amount of organic carbon received by the seafloor and that the fraction that is buried in the sediments decreases from south (58%) to north (27%). We further measured that more iron, an important micro-nutrient for algae growth, can be released from the seafloor the more organic carbon accumulates. Thus, sea ice conditions determine the organic carbon accumulation, turnover, and nutrient release at the seafloor, which are likely to be affected by future climate change.

1. Introduction

The biogeochemical properties of shelf sediments, such as organic matter (OM) content and degradation rates, serve as a reference point for the time-integrated organic carbon export from surface waters to the seafloor (Seiter et al., 2005; Smith et al., 2006). In the Antarctic, the amount of organic matter originating from surface primary production is highly variable – both temporally and spatially – due to seasonal sea ice cover and buoyancy production (i.e., stratification) and their effect on light regime and mixed layer depth (Savidge et al., 1995). The partial or complete retreat of sea ice cover in the spring–summer season allows light to become available for photosynthesis. When part of the ice melts, a stratified water column with nutrient-rich surface waters develops due to the input of sea-ice meltwater and suppressed wind mixing (Vernet et al., 2008). This strong stratification

forms a shallow summer mixed layer depth (5–25 m) (Garibotti et al., 2005; Vernet et al., 2008), which supports the growth of intensive phytoplankton blooms that usually follow the receding ice edge with a maximum production at the marginal ice zone (Savidge et al., 1995). A low production is observed in open waters of the Southern Ocean (SO), where a deepening of the summer mixed layer by wind forcing disperses macro- and micronutrients, such as Fe, and a deep mixing depth limits light availability (Vernet et al., 2008). On the other hand, the occurrence of sea ice cover reduces the light availability and thereby suppresses primary production. Thus, in Antarctic areas variations in sea ice cover and water column stability affect phytoplankton growth conditions and, ultimately, the carbon flux to the sea floor.

The deposition of pelagic production causes continental shelf sediments to be major sites of OM remineralization and nutrient regeneration in the ocean (Jahnke & Jackson, 1992). After OM reaches the seafloor, some of it is degraded and remineralized by microbes to form dissolved inorganic carbon, ammonium, silicate and phosphate, while the reduction of metal oxides releases adsorbed phosphate and micronutrients such as dissolved Fe, which are then potentially transported back to the water column (Billen, 1982; Wehrmann et al., 2014) and may fuel extensive phytoplankton blooms (Borrione et al., 2014; Hatta et al., 2013; Measures et al., 2013; Nielsdóttir et al., 2012; Venables & Meredith, 2009). Thus, shelf sediments play an important role in the benthic-pelagic coupling by providing essential nutrients for algae growth and maintaining the high primary production of shelf areas and the adjacent open ocean.

In the SO, which is known to be a high nutrient-low chlorophyll (HNLC) region, primary production is limited by low abundance of bioavailable iron (Boyd et al., 2007; Martin et al., 1990). The recycling of trace metals in Antarctic shelf sediments and their subsequent release into the water column could possibly represent an important source of bioavailable iron to the SO. According to Monien et al. (2014), Antarctic shelf sediments contribute up to 790 Gg a⁻¹ of bioavailable Fe, comparable to the contribution of iceberg-hosted material, which is assumed to contribute 180–1,400 Gg a⁻¹ of bioavailable Fe (Raiswell et al., 2016), whereas aeolian transport accounts for an input of less than 1.12 Gg a⁻¹ (Lancelot et al., 2009; Raiswell et al., 2016). In addition, a substantial release of dissolved Fe by anoxic subglacial meltwaters is estimated to range between 8.9 and 11,000 Gg a⁻¹, but only 0.03–5.9 Gg a⁻¹ of this bioavailable iron can reach oxic shelf waters when taking into account the rapid oxidation of dissolved Fe to Fe(III) (Wadham et al., 2013). The availability of shelf-derived micronutrients, in turn, is likely to be facilitated by the seasonal occurrence of a well-mixed water column promoting the upwelling of iron-enriched bottom waters, as shown for the Ross Sea (Collier et al., 2000; Sedwick et al., 2000). Further, significant lateral fluxes of Fe from the shelf of the Antarctic Peninsula and of sub-Antarctic islands to the Fe-poor Antarctic Circumpolar Current (ACC) have been reported by (Borrione et al., 2014; de Jong et al., 2012; Hatta et al., 2013; Measures et al., 2013; Nielsdóttir et al., 2012; Venables & Meredith, 2009). They argue that large quantities of this shelf-derived Fe were rapidly transported by the ACC and likely responsible for the extensive phytoplankton blooms in areas downstream of the Drake Passage. Thus, phytoplankton production in the circum-Antarctic and Southern Ocean may be substantially influenced by micronutrient regeneration (especially of iron) in shelf sediments of Antarctica and sub-Antarctic islands.

The Antarctic Peninsula is projected to undergo profound climatic and environmental changes (Vaughan et al., 2003) affecting seasonal sea ice cover, water column stratification, terrestrial melt water run-off and related nutrient input, and thus the conditions for primary production, organic carbon export and benthic remineralization. Our study serves two purposes, first to investigate and compare the present-day sediment biogeochemistry of the eastern continental shelf of the Antarctic Peninsula, especially OM remineralization and iron cycling, along a gradient of above-mentioned boundary conditions (sea ice cover, stratification), and second to provide a baseline of comprehensive geochemical data along a sea ice gradient from southern to northern stations that can be compared to future studies by revisiting the same sites.

Here, we report for the first time oxygen profiles and respective fluxes in combination with pore-water profiles of redox sensitive trace metals (Mn, Fe), nutrients (NO₃⁻, PO₄³⁻), sulfate and metabolic products (NH₄⁺, H₂S, DIC) from seven different locations along the eastern coast of the AP. These results are paired with solid-phase contents of total organic carbon (TOC), Mn, Fe, P and radioisotope ²¹⁰Pb data to provide a detailed picture of carbon fluxes, mineralization and burial as well as trace metal cycling under various environmental conditions. This includes the estimation of the total carbon re-mineralization rate as well as the contribution of the various electron acceptors to the overall OM degradation. The established fluxes are discussed in light of the boundary conditions for primary production, such as sea-ice cover and stratification. Moreover, we discuss geochemical conditions

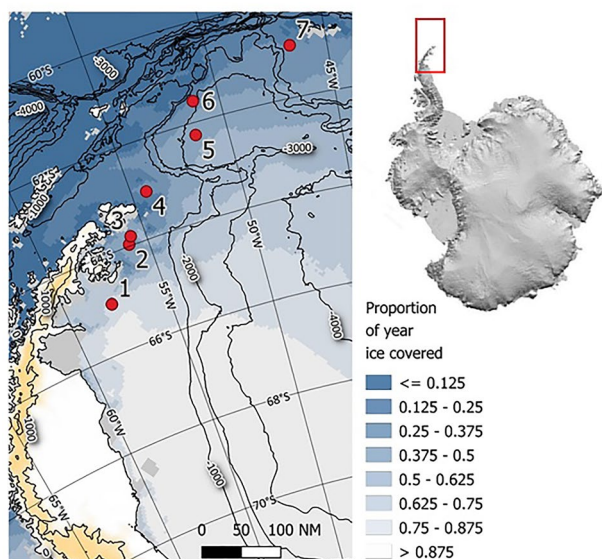


Figure 1. Map showing the Antarctic Peninsula with the locations of the sampled stations (red circles with station numbers) during PS118 expedition. Colors denote the proportion of time the ocean is covered by sea ice of concentration 85% or higher as calculated from AMSR-E satellite estimates of daily sea ice cover at 6.25 km resolution (Spren et al., 2008). Water depth is indicated by isolines.

and biogeochemical processes affecting the iron efflux from Antarctic shelf sediments as a potential source of bioavailable iron for the Southern Ocean.

2. Materials and Methods

2.1. Sample Collection

During the research cruise PS118 with the German research vessel RV POLARSTERN (Feb 2019–April 2019, Dorschel, 2019) sediments were collected from 7 stations along a 400 mile transect from the eastern shelf of the Antarctic Peninsula to the West of the South Orkney Islands (Figure 1, Table 1). At five stations, sediment samples were collected on the shelf at similar depths, ranging between 350–450 m, to allow cross-comparison of sediment properties independent from water depth. Another two stations were situated in the Powell Basin at 3,300 and 2,900 m, serving as deep sea reference. Prior to the sediment sampling, the water column was sampled by means of a conductivity-temperature-depth-probe (CTD, Seabird 911plus), equipped with an additional O₂ sensor (Sea-Bird SBE43) and a Rosette water sampler with 24 Niskin bottles of 12 L capacity.

At each station, a total of nine sediment cores with intact surface sediments and overlying water were collected from multiple deployments of a multicorer (Oktopus GmbH, Kiel, Germany). Immediately upon retrieval, sediment cores were transferred to the ship's cool laboratory and placed in a water bath at 0°C. Three cores were used for oxygen micro-profiles and whole core oxygen consumption measurements and three cores each were used for pore-water and solid phase analyses, respectively. Finally, 3–5 cores per station (usually cores used for pore-water sampling and oxygen measurements) were size-fractionated through 1,000, 500 and 300 μm sieves and the macrofauna (plus larger grains/stones) fixed in borax-buffered formaline (4% final concentration). For this study, the macrofauna was only visually inspected while a thorough determination of species abundance and diversity was not performed.

The pore-water was sampled with rhizon samplers (pore size 0.1 μm; Rhizosphere Research Products, Netherlands) within 1–2 hr after core retrieval (Seeberg-Elverfeldt et al., 2005). Samples were taken at depth resolutions of 1 cm from 0 to 10 cm and below 10 cm with a resolution of 2 cm down to a maximum depth of 30 cm. Subsamples for trace element analyses of dissolved iron (DFe) and manganese (DMn), for dissolved inorganic carbon (DIC), hydrogen sulfide (H₂S) and for nutrients such as ammonium (NH₄⁺), phosphate (PO₄³⁻), nitrate (NO₃⁻), nitrite (NO₂⁻) and silicate (SiO₃²⁻) were taken. For trace elements, the first 1 ml of extracted pore-water was discarded to ensure that the samples had not been in contact with air. Then, 1 ml of pore-water was taken and filled into 2 ml polypropylene (PP) tubes prefilled with 25 μl of 2% v/v of HCl and stored at 4°C. For DIC, 2.2 ml of pore-water was preserved with 10 μl of 10% HgCl₂ in brown glass vials without headspace and stored at 4°C. For nutrient, sulfate (SO₄²⁻) and chloride analyses, 4 ml of pore-water were filled into 15 ml plastic tubes and stored at –20°C. For H₂S analyses, 1.5 ml of pore-water was directly transferred into a 2 ml PP tube (Eppendorf, Germany) already filled with 0.6 ml of a 50 mM Zn acetate solution and stored at 4°C. Sediments of parallel cores were sampled for solid phase analyses at the same depth resolution and stored at –20°C. At 6 stations, additional seawater samples 5 m above the seafloor were obtained by using the CTD-rosette system.

2.2. Oxygen Uptake Measurements

High-resolution O₂ profiles were measured in the upper sediment layer using optical microsensors (Optodes, Pyrosience) in order to determine oxygen penetration depths and diffusive oxygen uptake (Table 1). For deep oxygen penetration depths (>5 cm), we used 430 μm bare fiber optodes glued into 20 cm long needles, while 50 μm thin retractable needle optodes were used for shallow oxygen penetration depths to increase the spatial resolution. Oxygen sensors were calibrated with 100% air saturation (air-bubbled sea water) and 0% air saturation (by adding sodium dithionite) at –1.0 ± 0.3°C and mounted on a motor-driven micromanipulator (MU1, Pyrosience). Temperature of the sediment core was recorded by a thermistor (Pyrosience) submersed into the overlying

Table 1
Characteristics of Sea Surface, Bottom Water (BW) and Sediment at the Sampled Stations

Station	Lon °E	Lat °N	Date DD/ MM/ YYYY	Water depth m	Ice cover %	Marg. sea ice index	WC-strat.				BW temperature °C	BW O ₂ concentration μmol L ⁻¹	NO ³⁻ -concentration μmol L ⁻¹	BW TOC wt%	OPD cm	DOU mmol m ⁻² d ⁻¹	TOU mmol m ⁻² d ⁻¹
							Δρ (50-5m) kg m ⁻³	salinity ‰	BW salinity ‰	BW Δρ							
1	-57.75	-64.98	04/03/2019	428	81	0.038	1.00	34.57	-1.9	308.60	32.921	32.921	0.71	6.31 ± 0.71 (7)	1.40 ± 0.27 (7)	2.15 (1)	
2	-55.90	-63.97	11/03/2019	415	49	0.127	0.27	34.54	-1.5	304.13	32.483	32.483	1.02	0.65 ± 0.08 (7)	3.54 ± 0.70 (8)	4.14 ± 1.16 (2)	
3	-55.74	-63.80	14/03/2019	455	47	0.084	0.19	34.54	-1.2	296.09	31.685	31.685	0.19	0.85 ± 0.18 (7)	1.75 ± 0.34 (9)	4.01 ± 1.10 (2)	
4	-54.33	-63.05	17/03/2019	447	33	0.174	0.16	34.56	-0.9	276.89	35.581	35.581	1.26	0.52 ± 0.07 (16)	6.87 ± 0.83 (16)	7.19 ± 0.44 (2)	
5	-51.42	-62.25	20/03/2019	3,295	46	0.122	0.28	34.63	-0.7	263.49	33.846	33.846	0.37	64.25 ± 0.58 (7)	0.18 ± 0.04 (7)	0.84 ± 0.25 (2)	
6	-51.13	-61.57	26/03/2019	2,908	34	0.121	0.10	34.64	-0.5	253.85	n. a.	n. a.	0.30	8.65 ± 0.26 (12)	0.24 ± 0.09 (10)	0.87 (1)	
7	-46.55	-60.93	28/03/2019	329	28	0.092	0.03	34.56	-0.1	250.09	34.651	34.651	0.60	1.87 ± 0.021 (15)	1.98 ± 0.84 (16)	1.77 ± 0.14 (2)	

Note. Ice cover (30 years average of daily sea ice cover), marginal sea ice index (occurrence of 5%–35% cover), upper water column stratification as density difference (Δρ) between 5 and 50 m depth. Total organic carbon (TOC) from the upper 5 cm depth. Oxygen penetration depth (OPD), diffusive oxygen uptake (DOU), and total oxygen uptake (TOU) data are presented as average ± SD with the number of measurements in parentheses. n.a.: not analyzed. At station 5, O₂ penetration was below the max. Possible O₂ profiling depth of 15 cm, so that the OPD was estimated by fitting to a model from Sachs et al. (2009).

water. A minimum of 3 profiles per core at randomly chosen positions were carried out in 100–500 μm vertical resolution from 4 mm above the sediment water interface down to 10–160 mm into the sediment. Profile data (depth, oxygen concentration, temperature) were recorded using a 4-channel FireSting oxygen meter (FSO2-4, Pyroscience) and processed using the “Profix” software from Pyroscience.

Volumetric oxygen consumption rates and diffusive oxygen uptake (DOU) was determined by inversely fitting the transport-reaction model PROFILE (Berg et al., 1998) to the measured oxygen concentration profiles. Oxygen diffusion coefficient in sediments was calculated according to Berg et al. (1998) as $D_s = \varphi^2 D$ where D is the diffusion coefficient of O_2 in seawater at 35 PSU and 0°C, and φ is the porosity of the sediment in the specific depth layer.

Two intact cores with undisturbed overlying water were used for whole core incubations to determine the total oxygen uptake (TOU). A plastic stopper was introduced into the core liner and pushed down to leave approximately 8–12 cm of water height above the sediment surface. The stopper was perforated with a hole to allow introducing a mini-optode (Pyroscience) from above. The overlying water in the cores was stirred by small magnetic bars mounted in the core liners and driven by a rotating magnet outside the cores. The cores were incubated in the water bath at controlled temperatures for at least 12 hr. Oxygen concentration was measured every 5 s using the 4-channel FireSting oxygen meter (FSO2-4, Pyroscience) and the software Pyro Oxygen Logger. Sediment total oxygen uptake rates were computed using linear regression of the O_2 concentration over time.

2.3. Pore-Water Analyses

All pore-water analyses were performed at the Alfred Wegener Institute, Helmholtz Centre for Polar and Marine Research (AWI) in Bremerhaven. NH_4^+ , NO_3^- , NO_2^- , PO_4^{3-} , and DIC were measured on a QuAatro four-channel flow injection analyzer (Seal Analytical). DFe, DMn were determined after a 10-fold dilution using Inductively Coupled Plasma Optical Emission Spectrometry (ICP-OES, Thermo iCAP7000) and yttrium internal standard solution used for calibration. The quantification limits of DFe and DMn were $0.143 \pm 0.143 \mu\text{M}$ and $0.036 \mu\text{M}$, respectively. Recoveries for DFe and DMn added in known concentrations to IAPSO Standard Seawater were $97.8 \pm 7.1\%$ and $100.7 \pm 7.6\%$, respectively. H_2S was analyzed using methylene blue method as described by Cline (1969). Sulfate (SO_4^{2-}) and chloride samples (1:100 dilutions with ultrapure water) were analyzed by ion chromatography (Metrohm IC Net 2.3).

2.4. Solid Phase Analyses

About 50 mg of freeze-dried and ground sediment was used for total nitrogen (TN), total carbon (TC) and TOC analyses in an Elemental analyzer (Vario EL III, Germany) equipped with a heat conductivity detector. For TOC contents, freeze-dried and homogenized sediment samples were decalcified using 0.5 ml of 37% HCl at 250°C for 2 hr and then measured by an Eltra CS-800 element analyzer. A soil calibration sample for CHNS (part no. 502-062, Leco, USA) and other internal standards were used for calibration. For the shelf stations (i.e., stations 1–4 and 7), a full acid digestion of freeze-dried and homogenized sediments was performed. Samples were treated with a mixture of 3 ml HCl, 2 ml HNO_3 and 0.5 ml HF and were heated and dissolved in a CEM Mars Xpress microwave system (e.g., Volz et al., 2020). Elemental contents were determined by ICP-OES, Thermo iCAP7000 analyses using an yttrium internal standard for correction of different ionic strengths. Recoveries for a total of nine processed sediment standards (MESS4) were $93.1 \pm 3\%$ for Al, $97.7 \pm 3\%$ for Fe (Fe total), $97 \pm 3\%$ for Mn, and $82 \pm 11\%$ for S. Sediment porosity was determined from water content, measured as weight loss after freeze drying and assuming a solid density of 2.6 g cm^{-3} as described by Burdige (2006).

2.5. Sedimentation Rate From ^{210}Pb

In order to determine and compare the sedimentation rates at all shelf stations (1–4 and 7), excess ^{210}Pb ($^{210}\text{Pb}_{\text{ex}}$) was measured in freeze-dried and homogenized sediments. The sample amounts used here ranged from 1 to 20 g, with most samples in the range of 4–10 g. The analyses was conducted on a planar HPGe gamma detector (Canberra/mirion). Sediment samples were weighed and sealed with hot glue in gas-tight petri dishes to prevent loss of ^{222}Rn ingrowing from ^{226}Ra . Samples were stored for >3 weeks to allow the relevant daughters of ^{226}Ra to grow into secular equilibrium before measurement. ^{226}Ra (for supported ^{210}Pb) was monitored via its

daughters ^{214}Bi and ^{214}Pb at lines 295, 351, and 609 keV. ^{210}Pb was measured at 46 keV, ^{241}Am at 59 keV, and ^{137}Cs at 661 keV. We do not report ^{241}Am and ^{137}Cs data because the peaks were only detected in a few instances, and were not sufficiently above background for a quantification. In profiles station 1–4, supported ^{210}Pb was set as the mean measured ^{226}Ra value because the scatter of the individual values due to analytical uncertainty was larger than the uncertainty in mean ^{226}Ra , which would have affected $^{210}\text{Pb}_{\text{ex}}$ in the older samples. For station 7, scatter in ^{226}Ra was small enough to subtract each individual ^{226}Ra value as supported ^{210}Pb . Samples were typically counted until approximately 1,000 net counts of ^{210}Pb were reached, or for maximum of three days if this number was not reached within this time period. Variable sample masses may affect detector efficiencies via self-absorption, especially at the low energy range of ^{210}Pb . This was addressed by determining mass-dependent efficiencies using IAEA-385 Irish Sea reference material for ^{210}Pb . No correction of the specific activities for salt was performed, as the cumulated dry mass is also determined including the salt component. Therefore, the inventory of ^{210}Pb , which is used for our preferred age model, is unaffected by salt in the samples.

The measurements were evaluated using the ScientiSiMe software, determining the age of samples according to the constant flux constant sedimentation model (CFCS) (Goldberg, 1963), the constant initial concentration model (CIC), and the constant rate of supply model (CRS) (Appleby, 2002; Appleby & Oldfield, 1978). The CRS model is insensitive to dilution, but sensitive to variations in sediment redistribution and to residual inventories below the sampling depth. Quite contrary, CIC is sensitive to dilution, but not to variable sediment redistribution or residual inventories. CFCS is not allowing for variations in lead flux or sedimentation rate. None of the approaches used here would correctly consider mixing due to bioturbation, with CFCS being probably the least affected. In general, we use in this study the CRS-age, taking the information from the other models into account for our interpretation.

2.6. Calculation of Sulfate Depletion

Sulfate depletion ($\text{SO}_4^{2-}\text{dep}$) in pore-water reflects the net amount of sulfate consumption via microbial SO_4^{2-} reduction in the sediments and was calculated according to Weston et al. (2006):

$$\text{SO}_4^{2-}\text{Dep} = \left(\frac{\text{Cl}^-_{\text{PW}}}{R_{\text{SW}}} \right) - \text{SO}_4^{2-}\text{PW} \quad (1)$$

where Cl^-_{PW} and $\text{SO}_4^{2-}\text{PW}$ are the measured concentrations of chloride and sulfate in the pore-water in mmol/L and R_{SW} is the molar ratio of Cl^- and SO_4^{2-} of seawater ($R_{\text{SW}} = 19.33$). Since the ratio of Cl^-_{PW} to R_{SW} reflects the expected SO_4^{2-} concentration in the pore-water at a given salinity, the difference between this concentration and $\text{SO}_4^{2-}\text{PW}$ provides an estimate for the amount of sulfate reduction.

2.7. Calculation of Pore-Water Diffusive Flux and Carbon Remineralization Rates

Besides oxygen uptake, fluxes of DFe, DMn, and NH_4^+ were estimated from the respective pore-water concentration gradients using Fick's first law of diffusion:

$$J = -\varphi D_s \frac{dC(z)}{dz} \quad (2)$$

in which J represents the flux of the specific solute and $dC(z)/dz$ represents the concentration gradient of the solute in a specific depth interval calculated by linear regression. Aerobic and anaerobic carbon remineralization rates (R_{aero} and R_{ana} in $\text{mmol C m}^{-2} \text{d}^{-2}$) were calculated from diffusive fluxes of O_2 , NH_4^+ , DFe and DMn considering the respective stoichiometric factors of the redox reactions (Froelich et al., 1979). Aerobic carbon remineralization (Equation 3) is calculated from the measured diffusive oxygen uptake subtracted by the re-oxidation of reduced reaction products (DFe, DMn, and S^{2-}) diffusing upward toward the oxic sediment layer. The total anaerobic remineralization was calculated from the upward flux of NH_4^+ ($J_{\text{NH}_4^+}$, Equation 4) multiplied by the C/N ratio of the organic matter. We used the NH_4^+ gradients below the NO_3^- penetration depth to exclude biases from anammox and/or bioturbation. The NH_4^+ gradients of 3 cores were used to calculate the average flux of NH_4^+ . Total remineralization rates of organic carbon (R_{tot} in $\text{mmol C m}^{-2} \text{d}^{-1}$) are calculated as the sum of aerobic and anaerobic rates (Equation 5).

$$R_{\text{aero}} = \frac{106}{138} J_{\text{O}_2} - \frac{1}{4} J_{\text{DFe}} - \frac{1}{2} J_{\text{dMn}} - 2 J_{\text{H}_2\text{S}} \quad (3)$$

$$R_{\text{ana}} = \frac{C}{N} J_{\text{NH}_4^+} \quad (4)$$

$$R_{\text{tot}} = R_{\text{aero}} + R_{\text{ana}} \quad (5)$$

From the DFe profile we calculated the upward flux using the DFe gradients above the DFe concentration peak. This needs to be distinguished from the total DFe flux which reflects the total net release of DFe and includes also the downward flux below the DFe peak. For comparison of concurrent PO_4^{3-} and DFe fluxes in the pore water, we calculate the flux ratio (J_P/J_{DFe}) from the respective pore-water gradients (dP/dz and $d\text{DFe}/dz$) and respective diffusion coefficients (D_P and $D_{\text{DFe}} = 2.46$ and $3.15 \times 10^{-10} \text{ m}^2 \text{ s}^{-1}$) in seawater at 0°C , (Boudreau, 1997):

$$\frac{J_P}{J_{\text{DFe}}} = \frac{-\varphi D_P \frac{dP}{dz}}{-\varphi D_{\text{DFe}} \frac{d\text{DFe}}{dz}} = \frac{D_P}{D_{\text{DFe}}} \frac{dP}{d\text{DFe}} = 0.78 \frac{dP}{d\text{DFe}} \quad (6)$$

where the ratio $dP/d\text{DFe}$ represents the slope of the linear regression between pore-water concentrations of PO_4^{3-} and DFe.

2.8. Calculation of Organic Carbon Supply Rate and Burial Efficiency

From the sedimentation rate (see above) the solid accumulation rate of the upper 2 cm is used in combination with the TOC content of the same layer to derive a TOC-accumulation rate for each station. In order to derive the total supply of organic carbon received by the sediments, the TOC removed in the upper layer due to aerobic C-remineralization is added to the TOC accumulation rate.

$$C_{\text{supply}} = \text{TOC}_{\text{accumulation}} + R_{\text{aero}} \quad (7)$$

The burial efficiency was also calculated for the individual station from the respective ratio of C-remineralization (R_{tot}) over C-supply as:

$$\text{Burial} = 1 - \frac{R_{\text{tot}}}{C_{\text{supply}}} \quad (8)$$

2.9. Calculation of Water Column Stratification and Sea Ice Cover

The conditions in the upper water column at time of sampling were characterized in terms of sea ice cover and water column stratification. Stratification was calculated from the density difference between 5 and 50 m water depth, $\Delta\rho = \rho_{50} - \rho_5$, measured on site with the CTD. In order to investigate how the measured water column stratification relates to the sea ice conditions encountered, the recent sea ice cover was calculated from satellite derived daily sea ice cover (0%–100%) at the stations, averaging a two-month interval prior the sampling date (Sea Ice Index, version 3, (Fetterer et al., 2017)).

From historic satellite data (Sea Ice Index, version 3, (Fetterer et al., 2017)), daily sea ice cover for the respective stations were extracted for the last 30 years (1990–2019) to calculate the long term mean sea ice cover (Table 1). To further characterize for each station the different degrees of sea ice cover over the season, each day of the 30 years of sea ice cover was classified as either no sea ice (<5%), marginal sea ice (5%–35%), dominant sea ice (35%–85%) and full sea ice (>85%), and their relative occurrence, weighted by the length of daylight (sunrise to sunset) was calculated to derive indices for the respective sea ice conditions.

3. Results

3.1. Sea Ice Conditions and Water Column Stratification

Long-term sea ice cover (Table 1) were found to decrease toward the North, from 81% (station 1) and ~47% (stations 2, 3, 5) to ~34% (stations 4, 6) and 28% (station 7). The stratification of the upper water column was strongest at station 1 with a density difference between 5 and 50 m of $\Delta\rho = 1 \text{ kg m}^{-3}$ and decreased toward station

7 down to $\Delta\rho = 0.03 \text{ kg m}^{-3}$ (Table 1). The density differences were dominated by changes in salinity, which were likely maintained by a combination of high fresh water inflow from ice melt and reduced wave mixing due to the sea ice cover. The water column stratification was therefore significantly correlated with the recent sea ice cover ($R^2 = 0.88$, $p < 0.001$), but also with long-term sea ice cover ($R^2 = 0.94$, $p < 0.001$).

Bottom-water salinity was between 34.54 and 34.64 PSU at all stations (Table 1). Bottom-water temperatures ranged from -1.9°C at station 1 to -0.1°C at station 7. All bottom waters were well-oxygenated with concentrations decreasing from $310 \mu\text{mol L}^{-1}$ (82% air saturation) at station 1– $250 \mu\text{mol L}^{-1}$ (70% air saturation) at station 7. Concentrations of bottom-water nitrate were between 33 and $35 \mu\text{mol L}^{-1}$.

3.2. General Characteristics of Sediments

Sediments consisted of silty clays to clayey silts across all stations, except for station 3, which contained a high fraction of fine sand (median grain size $116 \mu\text{m}$) and thus exhibited a low porosity of 0.42–0.48. Porosities of the other shelf stations ranged between 0.83 and 0.89 at the surface and 0.68–0.78 at 30 cm depth, whereas porosity of deep-sea sediments (stations 5 and 6) were between 0.55 and 0.75. Sediments of stations 1, 3, 5, 6, and 7 had a distinct brown color throughout the cored interval, whereas station 2 exhibited a 6 cm thick brown surface layer, below which the sediment color changed to gray. Sediment of station 4 was characterized by a blackish color and a sulfidic odor below 10 cm depth.

The mean TOC content in the upper 5 cm depth (Table 1) was lowest at the sandy station 3 (0.19 wt%) and at the deep stations 5 and 6 (0.37 wt% and 0.30 wt%). On the shelf, TOC increased from 0.71 wt% at the ice-covered station 1 to 1.02 wt% at the dominant sea ice station 2 and 1.26 wt% at the marginal sea ice station 4, and decreased thereafter to 0.60 wt% at the poorly ice-covered station 7. Except for station 3, which showed no trend with sediment depth, TOC content at 25–30 cm depth was significantly lower compared to the upper 5 cm, with values lowered by 15% (stations 5 and 6), 25% (stations 1, 4 and 7) and 45% (station 2). Molar C/N ratios at the sediment surface (0–5 cm) were between 8 and 9 for all stations, except for station 1, where values were above 10. At this station, C/N ratio decreased downward to 8 at 25–30 cm depth, while at all other stations the values slightly increased by 5%–15%.

Benthic macrofauna, when present, consisted mainly of polychaetes, bivalves, brittle stars, and few isopods. Considering the fraction larger than $1,000 \mu\text{m}$, station 1 showed the lowest fauna diversity and abundance compared to other stations. Stations 2 and 3 showed the highest density of benthic species with communities dominated by polychaetes and bivalves. Further, station 4 had a relatively high faunal density, dominated by small bivalves and brittle stars. On contrary, we found lots of empty polychaete tubes at station 7.

3.3. Dissolved Oxygen Flux and C-Remineralization Rates

Oxygen penetration depths (OPD) were 6.3 cm at station 1 and 8.7–64.2 cm at stations 6 and 5 (deep sea), reflecting low oxygen consumption in these sediments (Table 1, Figure 2). Stations 2, 3 and 4 were characterized by similar penetrations depths ranging between 0.85 and 0.52 cm. At station 7, the OPD slightly increased again to 1.9 cm. Repeated oxygen profiles were highly reproducible for each station and showed no signs of fauna burrows. High volumetric oxygen consumption rates were found either close to the sediment-water interface or near the OPD, indicating aerobic remineralization of fresh organic matter at the surface and re-oxidation of reduced solutes at the OPD. In general, the calculated diffusive oxygen uptake (DOU) corresponds to the OPD, showing low values of $1.4 \text{ mmol O}_2 \text{ m}^{-2} \text{ d}^{-1}$ at station 1 and $0.2 \text{ mmol O}_2 \text{ m}^{-2} \text{ d}^{-1}$ at stations 5 and 6, while increasing to 3.5 and $6.9 \text{ mmol O}_2 \text{ m}^{-2} \text{ d}^{-1}$ at stations 2 and 4. Due to the low porosity (0.48) of the sandy sediment at station 3, the DOU was as low as $1.8 \text{ mmol O}_2 \text{ m}^{-2} \text{ d}^{-1}$, despite the shallow OPD. At station 7, the DOU was found to be $2.0 \text{ mmol O}_2 \text{ m}^{-2} \text{ d}^{-1}$. The total oxygen uptake (TOU) corresponds to DOU and there was no significant difference between DOU and TOU, except for the sandy station 3 where total uptake was approximately twice the diffusive uptake.

From pore-water profiles of NH_4^+ , DFe, DMn and H_2S (Figure 3) respective fluxes were calculated and balanced with the DOU to derive aerobic, anaerobic and total C-remineralization rates (Table 2) according to Equations 3–5. Total C-remineralization was reduced to 0.14–0.18 $\text{mmol C m}^{-2} \text{ d}^{-1}$ in the deep sea. On the shelf, the rates ranged from 1.2 to $7.4 \text{ mmol C m}^{-2} \text{ d}^{-1}$ and are distributed similarly across the stations as for DOU.

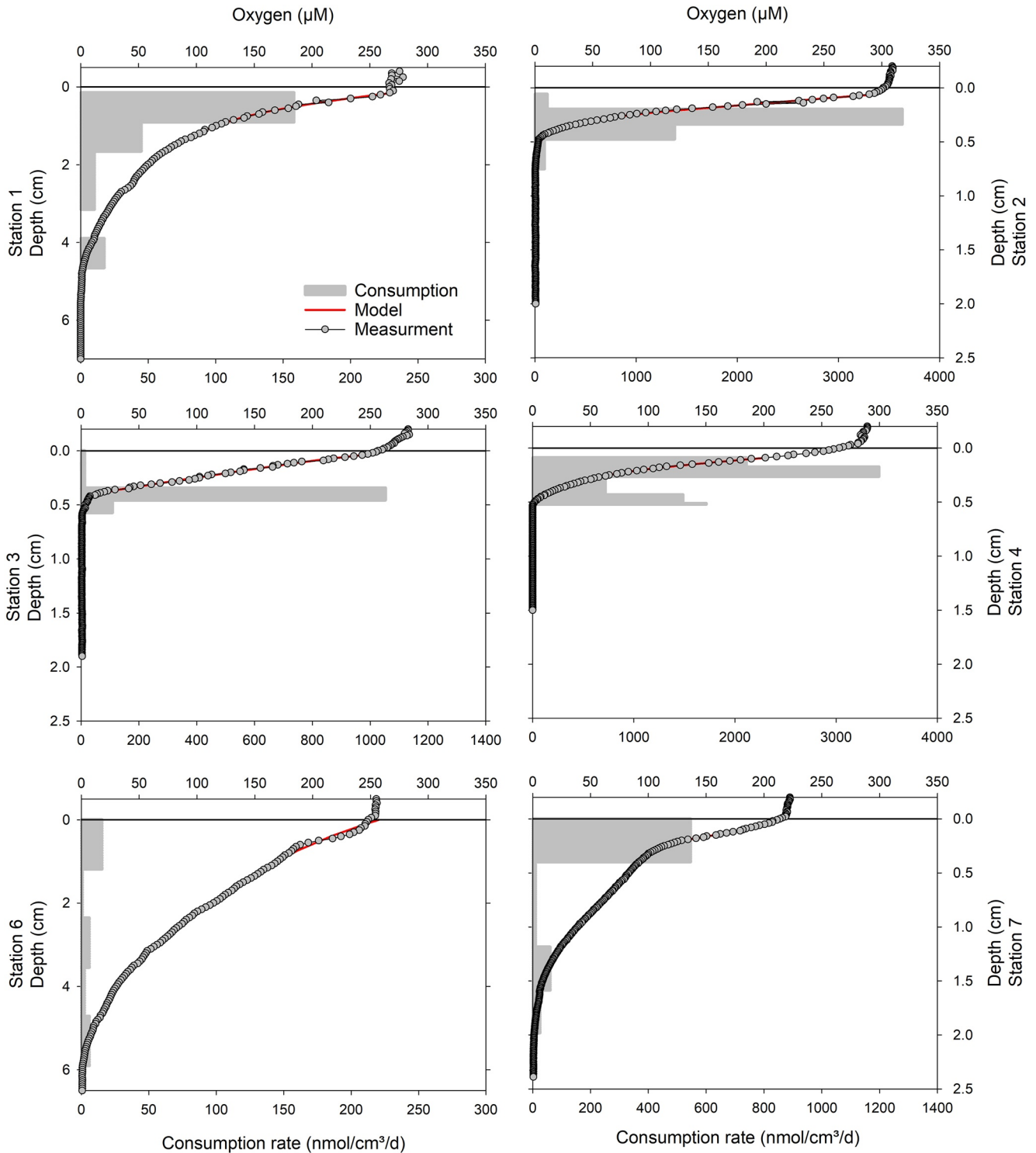


Figure 2. Representative O_2 profiles measured with optical microsensors for stations 1, 2, 3, 4, 6 and 7. The horizontal lines indicate the sediment surface. Gray circles mark measured O_2 profiles. Red lines are the modeled oxygen profiles and gray shaded boxes show the modeled consumption rate for specific depth intervals, both calculated using the transport-reaction model PROFILE (Berg et al., 1998). Note the different scales for the consumption rates and sediment depths.

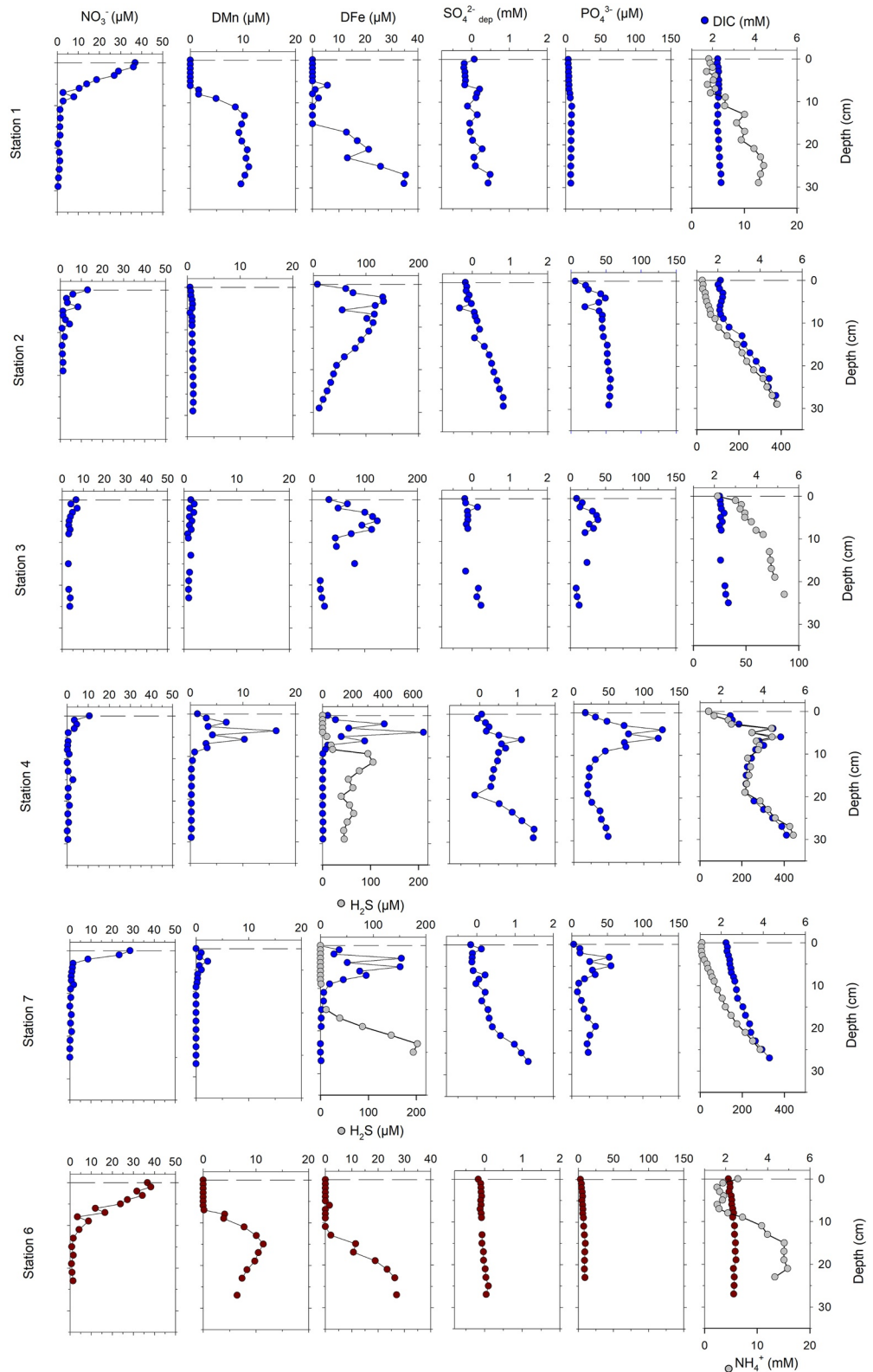


Figure 3. Representative profiles of reactive pore water compounds at the 5 shelf stations (blue) and 1 deep station (in red). SO_4^{2-} depletion profiles calculated based on the molar ratio of Cl^- and SO_4^{2-} of seawater (Equation 1). Note that the scale for DFe and NH_4^+ concentrations changes between stations. Free H_2S was present only at stations 4 and 7.

Table 2
The Rates of Aerobic, Anaerobic and Total Carbon Remineralization Were Calculated via Equations 2, 3, and 4

Station	C equivalents total aerobic remineralization rate		C equivalents total anaerobic remineralization rate		C equivalents total remineralization rate		Anaerobic C remineralization of total C		Fe reduction of anaerobic C remineralization		Net NH_4^+ flux		Net DFe flux		Upward DFe flux		Modeled DFe flux	
	$\text{mmol m}^{-2} \text{d}^{-1}$	$\text{mmol m}^{-2} \text{d}^{-1}$	$\text{mmol m}^{-2} \text{d}^{-1}$	$\text{mmol m}^{-2} \text{d}^{-1}$	$\text{mmol m}^{-2} \text{d}^{-1}$	$\text{mmol m}^{-2} \text{d}^{-1}$	%	%	%	%	$\text{mmol m}^{-2} \text{d}^{-1}$	$\text{mmol m}^{-2} \text{d}^{-1}$	$\text{mmol m}^{-2} \text{d}^{-1}$	$\text{mmol m}^{-2} \text{d}^{-1}$	$\mu\text{mol m}^{-2} \text{d}^{-1}$	$\mu\text{mol m}^{-2} \text{d}^{-1}$	$\mu\text{mol m}^{-2} \text{d}^{-1}$	$\mu\text{mol m}^{-2} \text{d}^{-1}$
Station 1	1.067	0.067	1.134	1.134	5.924	11.933	0.008 ± 0.004 (3)	0.032 ± 0.037 (3)	17.74 ± 0.018 (3)	0.62								
Station 2	2.699	0.409	3.108	3.108	13.145	3.871	0.043 ± 0.003(3)	0.063 ± 0.003 (3)	51.90 ± 0.008 (3)	1.74								
Station 3	1.330	0.122	1.452	1.452	8.389	14.573	0.014 ± 0.008 (3)	0.071 ± 0.073 (3)	58.00 ± 0.074 (3)	0.83								
Station 4	4.699	2.697	7.396	7.396	36.465	2.926	0.310 ± 0.223 (2)	0.316 ± 0.248 (2)	170.63 ± 0.140 (2)	4.54								
Station 5	0.136	-	0.136	0.136	-	-	-	-	-	0.09								
Station 6	0.183	0.016	0.199	0.199	8.165	2.081	0.002 (1)	0.001 (1)	0.00	-								
Station 7	1.314	0.519	1.833	1.833	28.301	3.277	0.057 ± 0.005(3)	0.068 ± 0.015 (2)	56.43 ± 0.051 (3)	1.25								

Note. Average fluxes of NH_4^+ , DFe, and upward DFe were estimated from pore water gradients and presented as average ± SD with the number of the total profiles in parentheses. Modeled benthic DFe flux to water column was calculated from bottom water oxygen concentrations (μM), and carbon remineralization rates using the equation from Dale et al. (2015).

At stations 4 and 7, a high contribution of anaerobic C-remineralization came from increased sulfate reduction rates as inferred from H_2S gradients (see below).

3.4. Pore-Water Chemistry

Pore-water profiles obtained at station 1 (81% sea ice cover) and station 6 (deep sea) show similar patterns (Figure 3), although station 1 has higher TOC contents (0.7%) compared to station 6 (0.3%). Nitrate concentrations gradually decrease from bottom water concentrations (37 μM) to zero within the uppermost 10 cm indicating denitrification under reducing conditions, just below the oxygen penetration depth. The relatively deep location of the nitrate reduction zone is in accordance with the moderate OM content. Concurrently, a steady downward increase of DMn concentrations (10 μM) caused by Mn(IV) reduction at a depth of 11 cm (and below) documents the metal reduction zone of these sediments. Furthermore, the downward increase of DFe concentration at a depth of 25–30 cm indicates the position of the Fe(III)-reduction layer. The deep and rather moderate increase of DFe is in line with a rather slow increase in nutrient concentration with depth (below 10 cm: <15 μM NH_4^+ , <10 μM PO_4^{3-} and <2.5 mM DIC) reflecting low microbial activity and nutrient recycling in these sediments. Furthermore, no clear evidence for a significant depletion in sulfate is found.

Pore-waters of station 2, which has an increased content of OM in the upper 5 cm (1.0% TOC, Table 1, Figure 4), show a more condensed redox zonation compared to station 1 and 6. We found complete nitrate consumption within 1–2 cm below the sediment surface. The nitrate reduction zone is followed by enhanced concentrations of DFe reaching a maximum of 133 μM in the first 5 cm. In contrast to station 1 and 6, the phosphate concentration (Figure 3) increases in the upper layer to a maximum of 50 μM at 5 cm depth. In this layer, phosphate concentrations significantly correlate with dissolved Fe concentrations, indicating co-precipitation and co-dissolution of phosphate and iron phases. The gradual increase in DIC to 4 mM and NH_4^+ to 400 μM indicates increased degradation of organic matter and nutrient release under progressively reducing conditions.

Station 3 has the lowest organic matter content (0.2% TOC) in the solid phase due to the high fraction of fine sand which also results in a low porosity. Nevertheless, reactivity in the pore space of the upper layer (0–5 cm) is comparable to station 2 with similar pore-water profiles of O_2 , NO_3^- , DFe and PO_4^{3-} concentrations. Further below the decreased gradients of DIC and NH_4^+ suggest that remineralization rates are limited by the organic matter content. The removal of dissolved Fe from the liquid phase in deeper sediment layers at station 2 and 3 strongly suggests sequestration of iron into sulfide minerals in these depths (>10 cm). This is confirmed by the sulfate depletion profiles showing increasing values with depth (station 2), whereas H_2S was not detected.

Pore-water profiles at station 4 show the characteristic sequence of typical redox zones, including the accumulation of H_2S in pore waters, as expected for sediment with high content of organic matter (1.3% TOC, Table 1). Nitrate is consumed within the first cm followed by a sharply bounded zone of dissolved Fe concentration peaking at 3–7 cm. This pattern is to some extent paralleled by dissolved Mn, however at 40-fold lower concentrations. Station 4 exhibits the highest concentrations of DFe (670 μM) found in all sampled sediments and, correspondingly, high phosphate concentrations of up to 125 μM significantly correlate with DFe concentrations. Further below, the removal of iron from the pore-water in deeper, more blackish sediments (>10 cm) marks the beginning of the sulfidic zone, where dissolved iron precipitates as iron sulfides. The upper part of the H_2S concentration profile was concave up, but further down the concentration showed an overall decrease with depth. At the base of the core, this is accompanied by a steady increase in SO_4^{2-} -dep (1.5 mM), DIC (4.5 mM), and NH_4^+ (443 μM) which

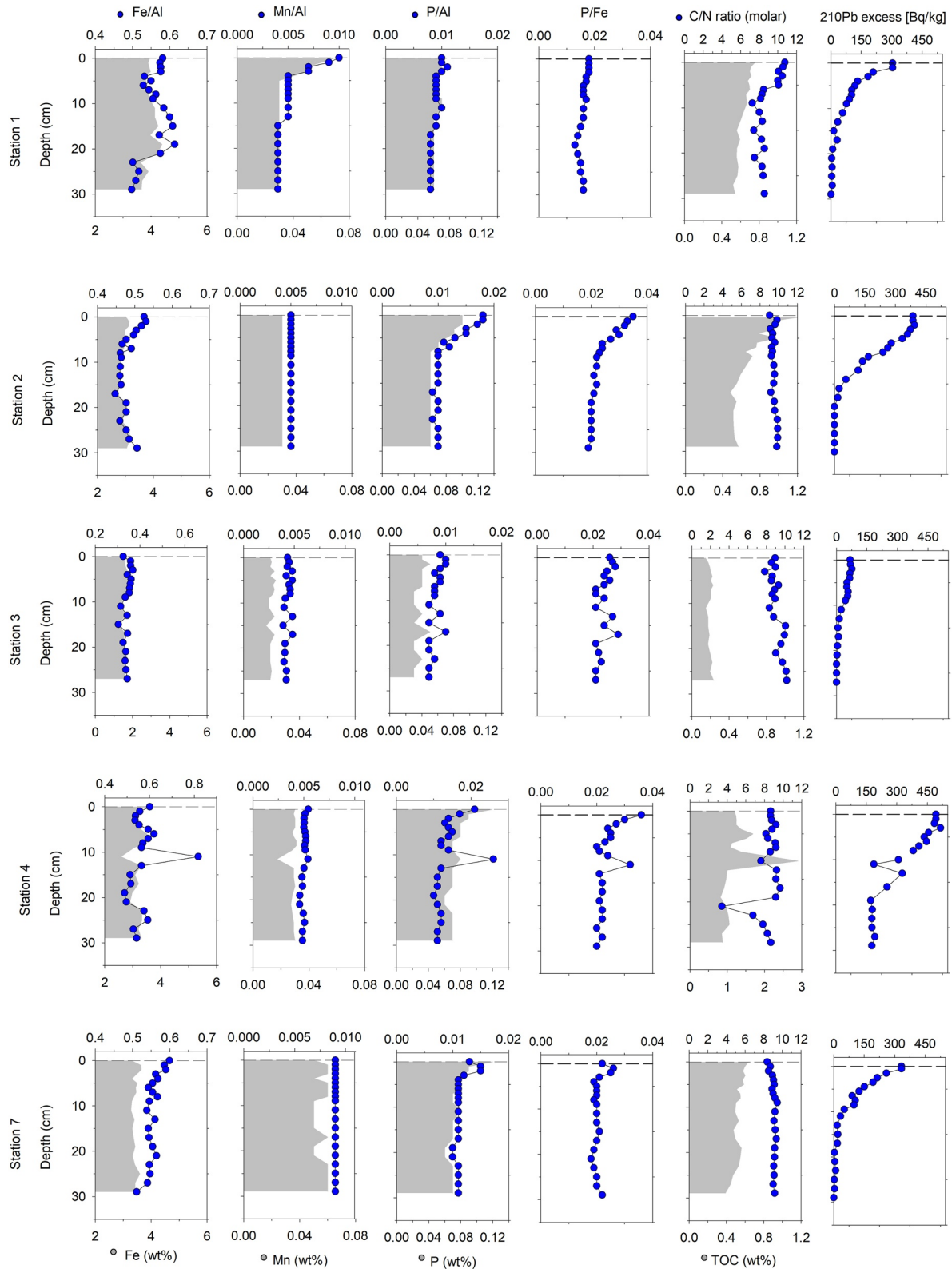


Figure 4. Detailed analysis of the solid phase for shelf stations. The total content of Fe, Mn and P is depicted as weight fraction (wt%) and normalized to aluminum. Further, the total organic carbon (TOC) and total nitrogen (TN) contents and excess activity of ^{210}Pb are shown.

suggest increased organic matter degradation at depth compared to the other sites. However, across the entire core the latter profiles show discontinuities, such as local maxima at 5 cm depth and minima at 20 cm depth, which coincide with local maxima (1.7 wt%) and minima (0.8 wt%) of the organic carbon content (Figure 4).

At station 7, the redox zonation is less condensed, showing NO_3^- penetration to 3 cm depth. Only low concentrations of dissolved Mn (max. 2.2 μM) are detected in the upper core, while DFe peaks at 5 cm depth with 150 μM , again well correlated with phosphate concentrations. Below the DFe peak, a gradual increase in SO_4^{2-} (1.2 mM) and the steep increase of H_2S concentration mark high sulfate reduction rates. Across the entire core, continuously increasing concentrations of DIC (max. 4.2 mM) and NH_4^+ (max. 285 μM) are similar to those of station 2 and correspond to continuously decreasing TOC contents (Figure 4).

3.5. Bulk Sedimentary Geochemistry

For shelf sediments (stations 1–4 and 7), the elemental composition of the solid phase was analyzed (Figure 4). Across stations and depths, Al/Ti ratios are relatively constant (14.8 ± 0.1 – 15.5 ± 0.1) confirming that both elements behave conservatively and are not affected by early diagenetic alterations. At all stations, Mn contents range from 0.02 wt% to 0.07 wt%, with Mn/Al ratios between 0.004 and 0.01. The Mn/Al ratio is stable at 0.005 at stations 2 and 4, while the coarse sandy sediment of station 3 results in lower Mn/Al ratio of 0.004. Station 7 exhibits elevated values of around 0.009. Variations with sediment depth are only found at station 1 where Mn content decreases downward from 0.010 to 0.005 within the uppermost 5 cm, just above the DMn increase in the pore-water (Figure 3), indicating Mn dissolution and re-precipitation.

The Fe contents range from 1.2 wt% to 4.5% with Fe/Al ratios of 0.3–0.62. Station 1 exhibits the highest Fe content (3.5–4.5 wt%) while station 3 shows low Fe contents (1.2–1.6 wt%). All other stations have values between 2.5 wt% and 3.5 wt%. The variation of Fe with sediment depth shows no clear trend, with the exception of stations 2 and 7, where an upward increase of Fe/Al is visible in the surface layer (0–5 cm). The P content ranges from 0.03 wt% to 0.12 wt%. Station 3 shows lowest values (0.03–0.04 wt%), while values between 0.06 wt% and 0.08 wt% are found at all other stations below 10 cm. Elevated P contents of up to 0.12 wt% are found at the surface of stations 2, 4 and 7. Normalization of Mn, Fe and P contents to the conservative Al contents emphasizes the depth dependent trends in elemental composition, showing the correlating trends of Fe/Al and P/Al in the surface sediments (0–5 cm) for station 2 and 4. An exception is found at station 4 in 10 cm depth, where a 3-fold higher TOC content indicates a change in sediment composition. At the same depth, Fe/Al, P/Al and S/Al (not shown) are elevated, indicating increased precipitation of Fe, S and P. This corresponds with the pore water profiles at the same depth where a sink for DFe from above and H_2S from below suggests the formation of iron sulfides (Figure 3).

3.6. Iron-Phosphate Cycling

In pore waters of all shelf stations, concentrations of DFe and PO_4^{3-} were significantly correlated in the surface layers at and above the DFe peak concentrations (Figure 5). The linear regression of the correlating values for stations 2, 3, 4 and 7 reveals a striking similarity with almost identical slopes between 0.33 and 0.35 $\mu\text{M PO}_4^{3-}$ per $\mu\text{M DFe}$. Only the correlation at station 1 showed a lower slope of 0.18 $\mu\text{M PO}_4^{3-}$ per $\mu\text{M DFe}$ (Figure 5). The slopes of the linear regressions are used to calculate flux-ratios of PO_4^{3-} over DFe (see Equation 6) of 0.14 for station 1 and between 0.26 and 0.28 for all other stations (Table 3).

The results of solid-phase contents of P and Fe are analyzed in a similar way (Figure 6). Despite the high background of Fe, the variations of P and Fe are nevertheless correlated with slopes between 0.18 and 0.37 mmol g^{-1} P per mmol g^{-1} Fe for stations 2, 4 and 7, showing a molar ratio similar to the flux ratios of PO_4^{3-} and DFe in the pore water. However, at stations 1 and 3, the slopes are 7-fold and 3-fold lower, respectively, at around 0.03 and 0.07 mmol g^{-1} P per mmol g^{-1} Fe (Figure 6, Table 3).

The range of variable Fe content for which the P-Fe correlation is detected (see example of drop lines in Figure 6) is between 1.4 and 4.1 mg Fe per gram solid and can be conservatively interpreted as the dynamic Fe fraction, which is accessible to Fe(III) reduction. When normalized by the total Fe content for each station, we can estimate that $9.0 \pm 3.3\%$ of total Fe content is accessible for Fe(III) reduction and takes part in the concurrent recycling

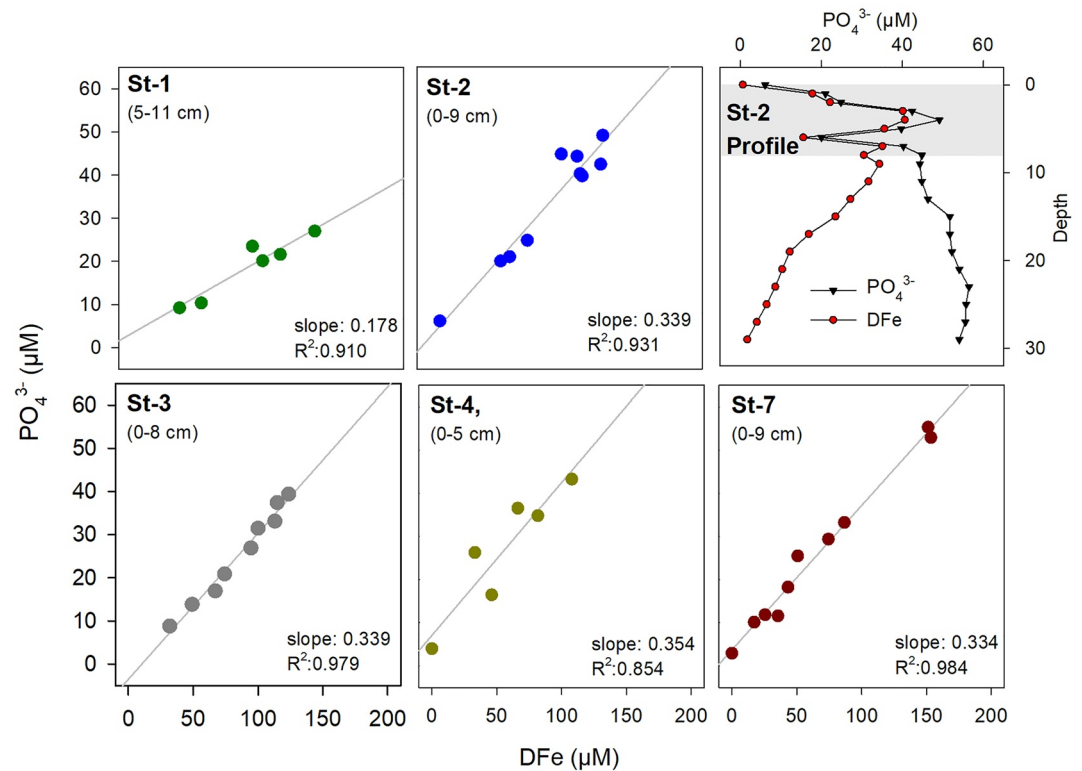


Figure 5. Correlation of PO_4^{3-} and DFe concentrations in the pore water of shelf stations. The relative standard error (RSE) of the slope is less than 10% ($p < 0.001$), except for station 4 (RSE $\sim 20\%$, $p < 0.01$). Upper right: example of correlating concentration profiles of DFe and PO_4^{3-} at station 2. The gray area marks the depth range of significant correlation.

of P and Fe (Table 3). The variable P content is calculated the same way and is estimated to make up $33 \pm 20.6\%$ of the total P content.

3.7. ^{210}Pb and Sedimentation Rates of OM and Iron

Profiles of excess activity of ^{210}Pb (Figure 4) indicate no bioturbation for station 1 and 7, whereas slight mixing of the upper 3–4 cm is indicated for stations 2, 3, and 4. Mean sedimentation rates, calculated from $^{210}\text{Pb}_{\text{ex}}$, range from 1.9 mm y^{-1} at station 1– 7.6 mm y^{-1} at station 4 (Table 3). The TOC accumulation ranges from 1.6 mmol C

Table 3
Detailed Analysis of Shelf Sediments

	Porewater Fe-P conc. ratio	Porewater P-Fe flux ratio	Solid P-Fe variability ratio	Solid-Fe recycled (accessible Fe) %	Solid-P recycled (accessible P) %	Sedimentation rate mm yr^{-1}	Solid acc. rate $\text{g m}^{-2} \text{d}^{-1}$	TOC acc. rate $\text{mmol m}^{-2} \text{d}^{-1}$	Total C supply rate $\text{mmol m}^{-2} \text{d}^{-1}$	Total Fe acc. rate $\text{mmol m}^{-2} \text{d}^{-1}$	Burial efficiency
Station 1	4.81	0.139	0.028	10.7	10.1	1.9	2.71	1.60	2.67	1.92	0.57
Station 2	2.65	0.264	0.237	13.1	58.8	2.2	4.82	4.08	6.78	2.60	0.54
Station 3	3.45	0.264	0.074	7.7	14.3	2.3	12.05	1.87	3.20	3.10	0.54
Station 4	2.15	0.276	0.367	4.3	43.1	7.6	7.91	8.27	12.97	4.67	0.43
Station 7	2.46	0.261	0.175	9.4	40.0	1.7	2.38	1.18	2.50	1.40	0.26

Note. The molar Fe:P pore water concentration ratios (calculated from the DFe peak position). P-Fe variability ratio in solids and pore water (flux ratio) and calculated fraction of accessible Fe and P in solids. Sedimentation rates (whole core averages, CFC model) from $^{210}\text{Pb}_{\text{ex}}$ analysis and accumulation rates of solids, TOC, particulate Fe, and the total carbon supply rate (=TOC accumulation + C-remobilization). Burial efficiency = $1 - (\text{C-remobilization}/\text{total carbon supply rate})$.

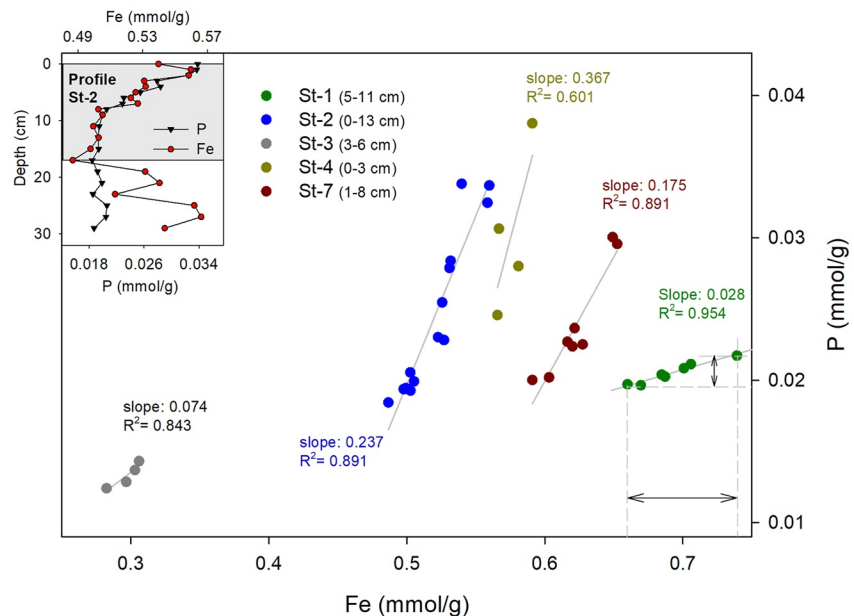


Figure 6. Correlation of P and Fe content in the solid phase of shelf stations. For stations 1, 2 and 7, the correlation was significant with a relative standard error (RSE) of the slope of 19% or less ($p < 0.005$). For station 3 (RSE = 30%, $p = 0.082$) and station 4, (RSE = 58%, $p = 0.22$) the correlation was not significant. The range of variable Fe and P content is indicated for station 1 by arrows between dashed drop-lines. The range was calculated for each station and used to estimate the percentage of Fe and P involved in the P-Fe recycling as presented in Table 3. Insert: example of correlating Fe and P content at station 2. The gray area marks the depth range of significant correlation.

$\text{m}^{-2} \text{d}^{-1}$ at station 1–8.3 $\text{mmol C m}^{-2} \text{d}^{-1}$ at station 4. Across all shelf stations these values are significantly correlated with the respective C-remineralization rate, independently derived from pore-water profiles (Figure 7a).

The supply rate of organic carbon ranges from 2.7 $\text{mmol C m}^{-2} \text{d}^{-1}$ at station 1–13.0 $\text{mmol C m}^{-2} \text{d}^{-1}$ at station 4. Across all shelf stations, a linear regression model relating the C-supply rate with the C-remineralization rate can be established (Figure 7a). The regression model can be fitted through the origin, as would be expected for a benthic C-remineralization that depends entirely on the C-supply rate. The slope of 0.54 implies that, on average, 54% of the organic carbon supplied to sediments on the shelf is mineralized, while 46% is preserved. Moreover, the burial efficiency, when calculated for each station according to Equation 8, decreased from station 1 (0.58) to station 7 (0.27) as bottom water temperatures increased from -1.9 to -0.1°C (linear correlation $R^2 = 0.92$).

Further, a significant linear relation (through the origin) is established between the total flux of DFe and the C-remineralization with a slope of 0.04 (Figure 7c). Considering a stoichiometry of 4 mole DFe released per mole C mineralized, we estimate that about 1% of the C-remineralization is coupled to Fe-reduction.

The solid accumulation rate is multiplied with the Fe content in the upper layer to derive the Fe-accumulation rate for each station (Table 3). The Fe accumulation ranges from 1.4 $\text{mmol Fe m}^{-2} \text{d}^{-1}$ at station 7 to 4.7 $\text{mmol Fe m}^{-2} \text{d}^{-1}$ at station 4. Across all shelf stations these values are neither correlated with upward flux nor total DFe flux (Figure 7d), suggesting that either the fraction of the Fe pool available for reduction varies between stations, or that Fe-reduction is not limited by Fe-sedimentation but mainly controlled by C-supply.

3.8. Carbon Fluxes Under Variable Sea-Ice Conditions

In order to relate the rates of C-remineralization and C-supply to conditions in the productive water layers above, we calculated sea ice indices for each station reflecting the relative frequency of different degrees of sea ice cover over the past 30 years, classified as no sea ice (<5% cover), marginal sea ice (5%–35%), dominant sea ice (35%–85%) and full sea ice (>85%). Only the occurrence of marginal sea ice cover (Table 1) was significantly correlated with the distribution of C-remineralization and C-supply rates of the shelf stations (Figure 7b). Marginal sea ice conditions combine both, favorable light conditions due to reduced sea ice cover and sufficient

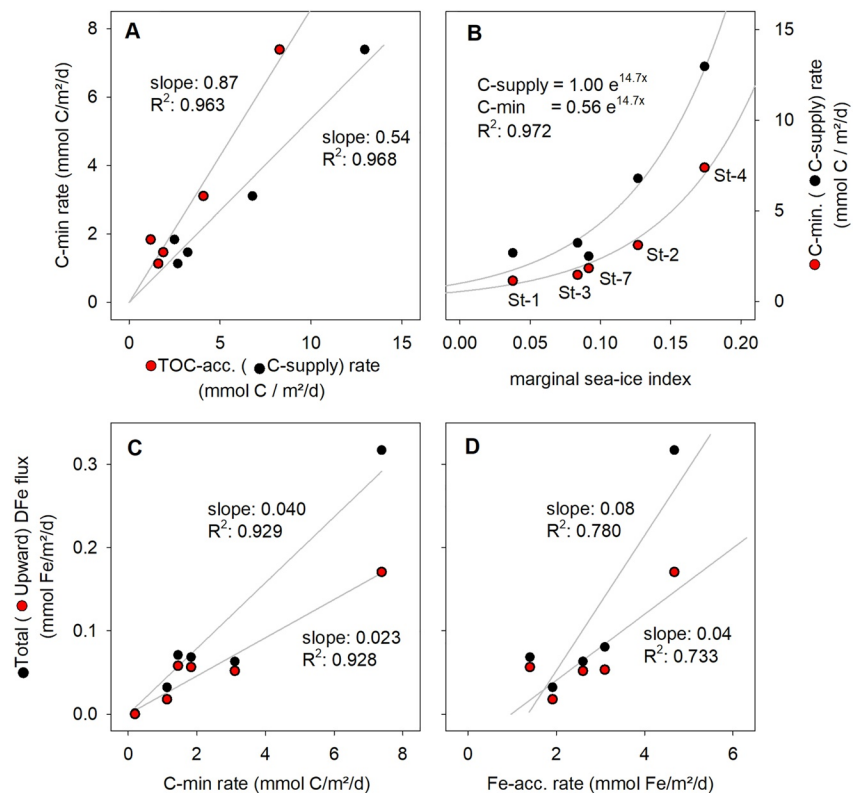


Figure 7. Relation between characteristic variables of shelf stations: (a) significant linear relationship between the independently measured values of C-remineralization and TOC-accumulation (red). Consequently, the C-supply rate (black) correlates as well (see Equation 7). The linear fit is forced through the origin, assuming that a constant proportion of 54% (see slope) of the C-supply is remineralized (RSE of slopes <6%, $p < 0.0001$). (b) The C-remineralization and C-supply rate as function of the marginal sea ice index (see text). The relationship is best explained by an exponential growth function with a global growth constant of 14.7 (RSE < 9%, $p < 0.0001$). The assumption for applying a growth function is that increasing periods of favorable sea-ice conditions lead to over-proportional primary production and, subsequently, over-proportional organic carbon supply of the sediments. (c) Significant increase of both, upward and total DFe flux as function of C-remineralization rates. The linear fit is forced through the origin, assuming that a constant proportion of 1% (see text) of C-remineralization is due to Fe-reduction (RSE of slopes <11% ($p \leq 0.0001$)). (d) The correlation between both upward and total DFe flux with the Fe accumulation rate in solids is not significant (RSE of slopes <30%).

buoyancy production by melt waters to establish a favorable stratification. Intriguingly, the relation between the marginal sea-ice index and C-supply (and C-remineralization) is best described by an exponential growth function, indicating that increasing periods of favorable sea-ice conditions lead to over-proportional rates of primary production and, subsequently, benthic carbon supply.

4. Discussion

4.1. Benthic Carbon Supply and Remineralization

We found low C-supply rates at stations that, on average, have either little light availability and strong summer stratification (heavy sea ice cover) or high light availability and little stratification (low sea ice cover). In contrast, intermediate stations with marginal sea ice cover (Figure 8) show a high C-supply rate. This suggests that primary production and export production is enhanced when both, light availability and stratification are sufficient to support a shallow critical mixing depth. Accordingly, a positive correlation between the measured C-supply rates with the marginal sea ice index (Figure 7b) was found, indicating that the shallow mixed layer depth at the marginal sea ice stations 2, 3 and 4 sustains primary production, yielding high C-supply rates of 7.6 mmol m⁻² d⁻¹ on average. An elevated primary production is reported for the marginal ice zone (MIZ) where ice melting also increases the supply of nutrients, iron in particular (Schloss et al., 2002), which further promotes surface primary production. In the coastal waters of the West Antarctic Peninsula, previous studies have attributed

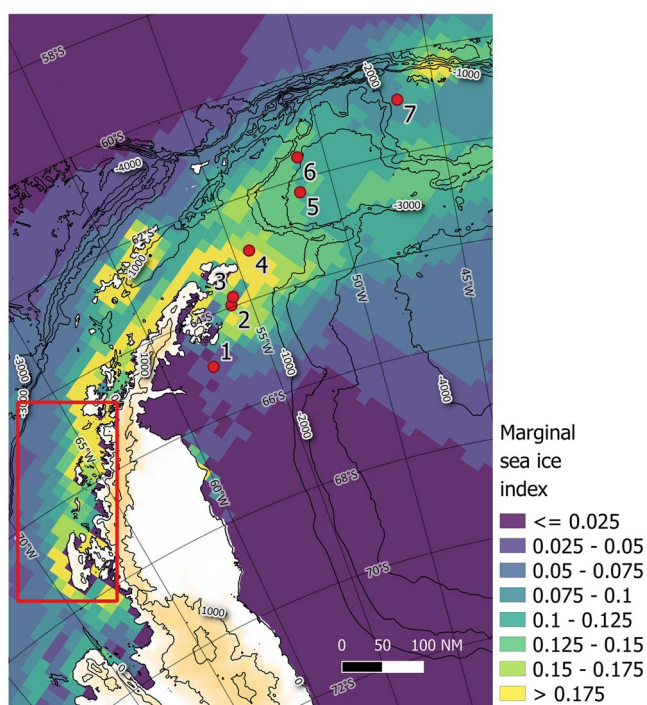


Figure 8. Map of marginal sea ice index, defined as relative occurrence of marginal sea ice cover (5%–35%), weighted by the length of daylight (sunrise to sunset). Values were derived from satellite data of daily sea ice cover from 1990 to 2019 at 25 km resolution (Fetterer et al., 2017). Sampling stations of this study are shown (red dots) as well as the study area of Garibotti et al. (2005) along the western shelf of the Antarctic Peninsula (red square). Isolines denote water depths.

high biomass (i.e., chl a) accumulation to light availability and shallow mixed-layer depths (Mitchell & Holm-Hansen, 1991; Sakshaug et al., 1991; Schloss et al., 2002), of usually <25 m (Garibotti et al., 2005), supporting our findings of high C- supply rates at the marginal sea ice stations. In fact, when our marginal sea ice index is calculated for a larger region (Figure 8), highest values of >0.2 coincide with elevated phytoplankton concentrations measured by Garibotti et al. (2005). In contrast, the ice-free station 7 (C-supply rate $2.5 \text{ mmol m}^{-2} \text{ d}^{-1}$) is exposed to wind-driven water-column mixing, which can deepen the mixed layer depth below the critical depth and thus reduce surface production, as found by Savidge et al. (1995). The occurrence of heavy sea ice cover at station 1 (C-supply rate to $2.6 \text{ mmol m}^{-2} \text{ d}^{-1}$) ultimately reduces the light availability and thereby suppresses primary production as found by Arrigo et al. (2008) and Bourgeois et al. (2017). As a consequence, the expected future changes in the sea-ice cover will influence the pelagic primary production, likely leading to a regional shift of marginal sea ice conditions and related high export of particulate organic carbon to shelf sediments.

The marginal ice-covered stations show an elevated TOC content (1.02–1.21 wt %) (Table 1) and high remineralization rates ($3.1\text{--}7.3 \text{ mmol m}^{-2} \text{ d}^{-1}$) (Table 2), supported by high C-supply rates. The C-supply to shelf sediments correlates with TOC content and carbon remineralization rates (Figure 7a), indicating that on average 54% of the received organic carbon is remineralized while 46% is preserved and buried to greater sediment depth. The positive correlation between C-supply rate and benthic carbon remineralization rate is consistent with many previous studies (e.g., Wenzhöfer & Glud, 2002) and thus a basic assumption for several models predicting benthic carbon mineralization in the ocean (e.g., Freitas et al., 2021; Middelburg et al., 1993; Zonneveld et al., 2010). The fraction of organic carbon that is buried/preserved in the uppermost sediments is high (27%–58%) but still in the range of reported burial efficiencies for marine sediments with comparable sedimentation rates (Canfield, 1994; Freitas et al., 2021; Katsev & Crowe, 2015).

However, we cannot exclude the effects of lateral sediment transport from areas adjacent to the sampled stations, which could have shifted the composition of the accumulated organic matter towards a higher refractory percentage. Lateral transport is indeed indicated by the ^{210}Pb inventories which were above the inventories expected for the region and water depths. However, a detailed analysis of this mismatch is out of the scope of this study and will be investigated elsewhere.

The organic carbon supply to the sediments is one of the major controls on sedimentary redox processes (Freitas et al., 2021; Seiter et al., 2005). The high organic carbon content determined at station 4 increases the relative importance of sulfate reduction (Jørgensen & Kasten, 2006), while the approximate net contribution of Fe reduction to anaerobic carbon remineralization is 3% at most. Thus, sulfate reduction is by far the major anaerobic carbon remineralization pathway contributing >30% to the total carbon remineralization. The dominance of sulfate reduction in anaerobic carbon remineralization agrees with the results of Nickel et al. (2008) who found that ice-free conditions along the northern Barents Sea support higher rates of sulfate reduction than found at the more permanently ice-covered stations which are characterized by lower carbon export to the sediment. In line with this, Wehrmann et al. (2014) found that in Arctic fjord sediments, high contents of reducible iron oxides combined with low contents of fresh organic matter lead to a dominance of dissimilatory iron reduction (DIR). We suggest that this is also the case at our stations 1, 2 and 3 with intermediate organic carbon contents of 0.71, 1.02 and 0.19 wt%. At these sites DIR could contribute about 4%–14% to the anaerobic carbon oxidation. It should be noted that we might overestimate the contribution of DIR since DFe can also derive from sulfide oxidation via Fe(III) reduction (e.g., Poulton et al., 2004; Wehrmann et al., 2017). Organoclastic sulfate reduction, which produces sulfide, might occur without being visible in the sulfate profile as diffusion pathways are short and the sulfate pool is quickly replenished in the uppermost centimeters of the sediment (Jørgensen et al., 2001). This pathway of DFe release increases with increasing TOC contents and the respective promotion of OM degradation

via sulfate reduction. In the end, however, the Fe liberation into pore water is always driven by OM degradation, either directly via DIR or indirectly via sulfide oxidation.

4.2. Controls on Benthic Iron Release

Primary production in many regions in the Southern Ocean is iron-limited (e.g., Boyd et al., 2007; Martin et al., 1990). The input of Fe into the surface waters of the Southern Ocean can enhance primary production resulting in a higher uptake of atmospheric CO₂ and enhanced organic matter deposition to the seafloor, that is, enhanced CO₂ sequestration (Boyd, 2002; Boyd et al., 2007; Death et al., 2014; Raiswell et al., 2008). Therefore, knowledge about the sources and the recycling of iron is of utmost importance. Recently, research studies have found that the Fe fluxes from coastal sediments are at least as significant as the input of iceberg-hosted material (Borrione et al., 2014; Hatta et al., 2013; Measures et al., 2013; Monien et al., 2014; Nielsdóttir et al., 2012; Venables & Meredith, 2009). Furthermore, Klunder et al. (2014) found that the elevated concentration of DFe in the WAP bottom water is mainly derived from shelf sediments. However, the contribution of benthic DFe efflux from deep shelf sediments to the bioavailable iron pool in the water column has not yet been sufficiently explored.

In the following, we discuss the DFe flux within the sediments as derived from pore-water profiles. This is not equivalent to the DFe efflux across the sediment-water interface, which is discussed thereafter. Our results show that upward and total DFe fluxes are significantly correlated with carbon remineralization rates (Figure 7c), explaining most of the variability in DFe fluxes, whereas the correlation of upward and total DFe fluxes with Fe-accumulation is not significant (Figure 7d). This finding agrees with Elrod et al. (2004) who found that benthic carbon remineralization rate is an important factor for predicting DFe fluxes. As mentioned above, the DFe liberation is driven by OM degradation – either directly via DIR or indirectly through organoclastic sulfate reduction and subsequent sulfide oxidation by Fe(III) reduction.

Measurements of DFe pore-water fluxes from polar continental shelf sediments are only available from a very limited number of studies (Henkel et al., 2018; Laufer-Meiser et al., 2021; Monien et al., 2014; Schnakenberg et al., 2021; Wehrmann et al., 2014). Comparison with existing data reveals that our estimated total DFe fluxes along the eastern coast of the Antarctic Peninsula are within the same range of the total DFe fluxes calculated for sediments from Potter Cove, King George Island, western Antarctic Peninsula (Monien et al., 2014). Including all stations of this study (Table 2), the resulting total DFe fluxes ranged between 0.032 and 0.316 mmol DFe m⁻² d⁻¹, which is comparable to the range of 0.011–0.424 mmol DFe m⁻² d⁻¹ estimated for Potter Cove sediments (Monien et al., 2014).

Both upward and total fluxes of DFe in the sediment were elevated at the marginal sea ice stations while moderate fluxes were observed at ice-free and ice-covered stations, respectively. At the marginal sea ice stations, the steep concentration gradients of DFe close to the sediment surface indicate that more DFe might escape from shelf sediments into the water column. Further, the high availability of easily reducible Fe oxides at the marginal sea ice stations favor Fe-reduction over organoclastic sulfate reduction as found in other continental shelf environments (Henkel et al., 2018; Herbert et al., 2021; Oni et al., 2015; Schnakenberg et al., 2021; Wunder et al., 2021). We assume that the majority of easily reducible Fe is derived from re-oxidation/precipitation of upward diffusing DFe at the Fe(II)/Fe(III) redox boundary. A similar pattern of easily reducible Fe through benthic iron cycling was found in Arctic fjord sediments (Laufer-Meiser et al., 2021). Furthermore, high accumulation rates of detrital inputs from rock weathering and erosion may represent additional sources of easily reducible Fe (Laufer-Meiser et al., 2021). How much of the Fe-reduction is fueled by recycled iron oxides depends on the spatial distance of the DFe source (i.e., location of Fe-reduction) to the DFe sinks above (re-oxidation) and below (FeS formation) as they shape respective gradients and fluxes. Similar upward and downward gradients of DFe as observed at station 4 (Figure 3) suggest that only about half of the reduced Fe is recycled, while at station 2 more than 80% of the reduced Fe is diffusing upwards toward the oxic layer. This corresponds to the solid phase analyses (Table 3) where we calculated a significantly higher percentage of recycled solid-Fe for station 2 (10.1%) compared to station 4 (4.3%).

Quantifying the DFe-efflux into the water column from DFe profiles is compromised by the re-oxidation/precipitation of DFe in the thin oxic layer. This oxidative trap prevents the transfer of most of the sediment sourced DFe to oxic bottom waters. The resolution of pore-water profiles is too coarse to resolve the partition between DFe-efflux and DFe-recycling, so that we employ a model from Dale et al. (2015) to calculate the DFe efflux across the

sediment-water interface using carbon remineralization rates (C_{\min} in $\text{mmol m}^{-2} \text{d}^{-1}$) and O_2 concentrations (O_2 in μM) in bottom water:

$$\text{DFe efflux} = \gamma \tanh\left(\frac{C_{\min}}{\text{O}_2}\right) \quad (9)$$

where γ ($= 170 \mu\text{mol m}^{-2} \text{d}^{-1}$) is the maximum DFe efflux for sediments at steady state located away from river mouths (Dale et al., 2015). The estimated benthic DFe efflux on the shelf ranges from 13 to 93 $\text{mg Fe m}^{-2} \text{yr}^{-1}$ (or $0.62 \mu\text{mol m}^{-2} \text{d}^{-1}$ to $4.54 \mu\text{mol m}^{-2} \text{d}^{-1}$, Table 2), which is 30–70 times lower than the upward DFe fluxes derived from DFe concentration gradients. The modeled DFe efflux scales primarily with the C-mineralization as it is the most variable model input (DFe efflux $= 6.1 \cdot 10^{-4}$ C-mineralization, $R^2 = 0.99$). Together with the previously described correlation of carbon remineralization rate and marginal sea ice index, we can now link sea-ice conditions and organic matter export to the potential release of DFe from the seafloor.

4.3. Coupled Iron-Phosphate Cycling

The presence of phosphate can have pronounced effects on the formation and types of Fe minerals and thus on the rate of microbial Fe-reduction (O'Loughlin et al., 2021). As organic matter is remineralized, phosphate is released into adjacent pore waters and diffuses upward where it may be released to bottom waters or is sequestered via sorption on primary and secondary Fe-oxide minerals (e.g., Paytan & McLaughlin, 2007). During sediment accumulation, reactive Fe-oxides and adsorbed (or co-precipitated) PO_4^{3-} are gradually buried until they reach the Fe reduction zone where Fe oxides are reductively dissolved releasing both DFe and PO_4^{3-} into the pore-water (Canfield et al., 1993; Holmkvist et al., 2010; Küster-Heins, de Lange, et al., 2010; Küster-Heins, Steinmetz, et al., 2010; März et al., 2018; Niewöhner et al., 1998). This redox Fe-cycling between oxidized and reduced Fe mainly controls the PO_4^{3-} flux and can promote the formation of secondary, poorly crystalline Fe (oxyhydr-) oxide minerals at the Fe redox boundary (Slomp et al., 1996), which are characterized by a high surface area and high reactivity (Canfield et al., 2006) that can adsorb significant amounts of PO_4^{3-} . In deeper sediments, the reductive release of DFe and PO_4^{3-} can be directly linked to the formation of fluorapatite and vivianite (März et al., 2008, 2018).

The significant correlation of phosphate and DFe concentration profiles at all shelf stations indicates a tight coupling of P and Fe cycles (Figure 5). The molar DFe: PO_4^{3-} concentration ratios calculated from pore-water profiles at the DFe peak position ranged between 2.1 and 4.8 (Table 3), a ratio which was reported to indicate that the majority of PO_4^{3-} release is closely associated with the reduction of iron (oxyhydr-) oxides (Küster-Heins, de Lange, et al., 2010; Küster-Heins, Steinmetz, et al., 2010; Kraal et al., 2019, 2020; Noffke et al., 2012; Slomp et al., 1996; Voegelin et al., 2013). Below the iron reduction zone, lower DFe: PO_4^{3-} ratios were observed suggesting the presence of a DFe sink (FeS formation) and the continuing release of PO_4^{3-} from organic matter remineralization (Niewöhner et al., 1998; Schulz et al., 1994; Wunder et al., 2021) and/or desorption from Fe-minerals. Similar trends of pore-water profiles of PO_4^{3-} and DFe have previously been observed in the Arctic marginal sea ice zone (Tessin et al., 2020), in the Peruvian oxygen minimum zone (Noffke et al., 2012), in sediments off Namibia (Küster-Heins, de Lange, et al., 2010; Küster-Heins, Steinmetz, et al., 2010) and in shelf sediments of the sub-Antarctic island of South Georgia (Wunder et al., 2021).

Intriguingly, the relative fluxes of PO_4^{3-} and DFe in the upper sediment of the sites investigated in this study, as calculated from the respective pore-water concentration (Figure 5, Equation 6), were almost identical at four of the five shelf stations with PO_4^{3-} /DFe flux ratios ranging between 0.261 and 0.276 (Table 3). Further, similar P/Fe ratios were detected in the sedimentary solid phase, although impaired by larger relative standard errors (Figure 6). The measurements indicate that the Fe-oxides carry a fixed proportion of phosphate, which is liberated upon Fe reduction. The proportion of ~ 0.26 may represent the upper phosphate incorporation capacity of the respective Fe-oxides. Voegelin et al. (2013) measured the dynamic phosphate incorporation into Fe(III)-precipitates during continuing Fe(II) oxidation and described the formation of phosphate-rich hydrous ferric oxide (HFO-P) with a similar maximum P/Fe ratio of 0.25. A high degree of Fe-recycling in our sediments may support the buildup of a large pool of such HFO-P which then imprints a P/Fe ratio of 0.25 onto the pore-water fluxes. To our knowledge it is quite unique for field measurements to provide such consistent evidence for the experimentally derived P sorption capacity. Only at station 1, the P/Fe ratio of 0.17 deviates from all other shelf stations. We speculate that the pool of HFO-P at station 1 is reduced because the Fe reduction rate is low (Table 2) compared to the

Fe-accumulation rate (Table 3), which also explains that the Fe content is 25% higher compared to the other shelf stations (~4 wt%, Figure 4). Further investigations on the formation/dissolution of P-Fe co-precipitates in surface sediments are important, especially for the Southern Ocean, to assess their impact on the P and Fe efflux into the water column.

5. Conclusions and Outlook

This study provides insight into benthic biogeochemical cycles and benthic carbon remineralization rates along a 400 mile transect from the eastern shelf of the Antarctic Peninsula to the West of the South Orkney Islands with different sea ice cover. Based on our estimates, carbon remineralization rates increased gradually from the heavy ice-covered station to the marginal sea ice stations from 1.1 to 7.3 mmol C m⁻² d⁻¹, respectively. The rates decreased again to 1.8 mmol C m⁻² d⁻¹ at the ice-free station, likely driven by a deeper water column mixed layer depth, which decreases primary production and thus organic carbon export to the sediment. Iron cycling in the sediment was highest at the marginal sea ice stations where Fe-reduction led to total DFe fluxes in the pore-water of up to 0.316 mmol DFe m⁻² d⁻¹, while moderate fluxes were observed at ice-free and ice-covered stations, respectively. In pore waters, concentrations of DFe and PO₄³⁻ were significantly correlated with almost identical flux ratios of 0.26 mol PO₄³⁻ per mol DFe for most of the stations, indicating a strong control of iron redox cycling on the phosphate release to the water column. The high benthic fluxes of DFe and PO₄³⁻ highlight the importance of sediments underlying the marginal ice zone as source for limiting nutrients to the shelf waters.

We propose that the extent and duration of sea ice cover are important in maintaining a preferential water column stratification and light regime for primary production and organic carbon export to the seafloor. As the iron, carbon and phosphate cycles are tightly linked, not only by primary production but also by carbon remineralization and sedimentary Fe redox cycling, changes in sea ice cover may affect both the biological carbon pump and the function of sediments as a potential source of iron and phosphate to the water column.

Recently, the Antarctic sea ice cover showed a drastic decline after 2015 hinting toward increased interannual variability (Eayrs et al., 2021) and eventually a continuous decline in the near future. Although a (southward) shift of areas with marginal sea ice cover can be expected, the impact on benthic processes depends on the site-specific seasonal dynamics of sea ice cover. For regions in which the MIZ is rapidly changing position with seasonal sea ice growth and retreat, favorable conditions for primary production pass quickly and the impact of climatological changes on the sediments might be low compared to our study area where the seasonal position of the MIZ is relatively stable, sufficient to leave a clear imprint on the benthic turnover.

Data Availability Statement

Data presented in this study are deposited at PANGAEA (Baloza et al., 2022), accessible under doi: <https://doi.org/10.1594/PANGAEA.942455>.

Acknowledgments

We acknowledge the help and effort made by the captain and crew members of RV POLARSTERN during Expedition PS118. We further thank Henning Schröder and Axel Nordhausen for preparing the multicorer and executing the deployment and recovery during the expedition. Special thanks go to Juliane Müller (AWI Bremerhaven) for carbon and nitrogen analyses of the sediments. Moreover, we gratefully acknowledge the help of Ingrid Stimac and Ingrid Dohrmann (AWI Bremerhaven) in the laboratory analyses. We also would like to thank Claudio Richter for his guidance while collecting macrofauna samples. We thank Peter Kraal, Alexander Michaud and another anonymous reviewer for their supportive and valuable comments. This study was funded by the AWI Grant-No. AWI_PS118_05. Open Access funding enabled and organized by Projekt DEAL.

References

- Appleby, P. G. (2002). Chronostratigraphic techniques in recent sediments. In *Tracking environmental change using lake sediments* (pp. 171–203). Springer.
- Appleby, P. G., & Oldfield, F. (1978). The calculation of lead-210 dates assuming a constant rate of supply of unsupported 210Pb to the sediment. *Catena*, 5(1), 1–8. [https://doi.org/10.1016/s0341-8162\(78\)80002-2](https://doi.org/10.1016/s0341-8162(78)80002-2)
- Arrigo, K. R., van Dijken, G., & Pabi, S. (2008). Impact of a shrinking Arctic ice cover on marine primary production. *Geophysical Research Letters*, 35(19), L19603. <https://doi.org/10.1029/2008gl035028>
- Baloza, M., Henkel, S., Geibert, W., Kasten, S., & Holtappels, M. (2022). Oxygen profiles, pore-water geochemistry and solid phase data of surface sediments retrieved from the eastern continental shelf of the Antarctic Peninsula. *PANGAEA*. <https://doi.org/10.1594/PANGAEA.942455>
- Berg, P., Risgaard-Petersen, N., & Rysgaard, S. (1998). Interpretation of measured concentration profiles in sediment pore water. *Limnology and Oceanography*, 43(7), 1500–1510. <https://doi.org/10.4319/l0.1998.43.7.1500>
- Billen, G. (1982). Modelling the processes of organic matter degradation and nutrients recycling in sedimentary systems. *American Journal of Science*, 282(4), 512–541. <https://doi.org/10.2475/ajs.282.4.512>
- Borriene, I., Aumont, O., Nielsdóttir, M. C., & Schlitzer, R. (2014). Sedimentary and atmospheric sources of iron around South Georgia, Southern Ocean: A modelling perspective. *Biogeosciences*, 11(7), 1981–2001. <https://doi.org/10.5194/bg-11-1981-2014>
- Boudreau, B. P. (1997). *Diagenetic models and their implementation* (Vol. 410). Springer.
- Bourgeois, S., Archambault, P., & Witte, U. (2017). Organic matter remineralization in marine sediments: A Pan-Arctic synthesis. *Global Biogeochemical Cycles*, 31(1), 190–213. <https://doi.org/10.1002/2016gb005378>
- Boyd, P. W. (2002). Environmental factors controlling phytoplankton processes in the Southern Ocean. *Journal of Phycology*, 38(5), 844–861. <https://doi.org/10.1046/j.1529-8817.2002.t01-1-01203.x>

- Boyd, P. W., Jickells, T., Law, C. S., Blain, S., Boyle, E. A., Buesseler, K. O., et al. (2007). Mesoscale iron enrichment experiments 1993-2005: Synthesis and future directions. *Science*, 315(5812), 612–617. <https://doi.org/10.1126/science.1131669>
- Burdige, D. J. (2006). *Geochemistry of marine sediments*. Princeton University Press.
- Canfield, D. E. (1994). Factors influencing organic carbon preservation in marine sediments. *Chemical Geology*, 114(3–4), 315–329. [https://doi.org/10.1016/0009-2541\(94\)90061-2](https://doi.org/10.1016/0009-2541(94)90061-2)
- Canfield, D. E., Rosing, M. T., & Bjerrum, C. (2006). Early anaerobic metabolisms. *Philosophical Transactions of the Royal Society B: Biological Sciences*, 361(1474), 1819–1836. <https://doi.org/10.1098/rstb.2006.1906>
- Canfield, D. E., Thamdrup, B., & Hansen, J. W. (1993). The anaerobic degradation of organic matter in Danish coastal sediments: Iron reduction, manganese reduction, and sulfate reduction. *Geochimica et Cosmochimica Acta*, 57(16), 3867–3883. [https://doi.org/10.1016/0016-7037\(93\)90340-3](https://doi.org/10.1016/0016-7037(93)90340-3)
- Cline, J. D. (1969). Spectrophotometric determination of hydrogen sulfide in natural waters. *Limnology and Oceanography*, 14(3), 454–458. <https://doi.org/10.4319/lo.1969.14.3.0454>
- Collier, R., Dymond, J., Honjo, S., Manganini, S., Francois, R., & Dunbar, R. (2000). The vertical flux of biogenic and lithogenic material in the Ross Sea: Moored sediment trap observations 1996–1998. *Deep Sea Research Part II: Topical Studies in Oceanography*, 47(15–16), 3491–3520. [https://doi.org/10.1016/S0967-0645\(00\)00076-x](https://doi.org/10.1016/S0967-0645(00)00076-x)
- Dale, A. W., Nickelsen, L., Scholz, F., Hensen, C., Oschlies, A., & Wallmann, K. (2015). A revised global estimate of dissolved iron fluxes from marine sediments. *Global Biogeochemical Cycles*, 29(5), 691–707. <https://doi.org/10.1002/2014gb005017>
- Death, R., Wadham, J. L., Monteiro, F., Le Brocq, A. M., Tranter, M., Ridgwell, A., et al. (2014). Antarctic ice sheet fertilises the Southern Ocean. *Biogeosciences*, 11(10), 2635–2643. <https://doi.org/10.5194/bg-11-2635-2014>
- de Jong, J., Schoemann, V., Lannuzel, D., Croot, P., de Baar, H., & Tison, J.-L. (2012). Natural iron fertilization of the Atlantic sector of the Southern Ocean by continental shelf sources of the Antarctic Peninsula. *Journal of Geophysical Research*, 117(G1). <https://doi.org/10.1029/2011jg001679>
- Dorschel, B. (2019). The expedition PS118 of the research vessel POLARSTERN to the Weddell Sea in 2019. In *Berichte zur Polar- und Meeresforschung = Reports on Polar and Marine Research* (Vol. 735, pp. 1–149). Alfred-Wegener-Institut, Helmholtz-Zentrum für Polar- und Meeresforschung. https://doi.org/10.2312/BzPM_0735_2019
- Eayrs, C., Li, X., Raphael, M. N., & Holland, D. M. (2021). Rapid decline in Antarctic sea ice in recent years hints at future change. *Nature Geoscience*, 14, 460–464. <https://doi.org/10.1038/s41561-021-00768-3>
- Elrod, V. A., Berelson, W. M., Coale, K. H., & Johnson, K. S. (2004). The flux of iron from continental shelf sediments: A missing source for global budgets. *Geophysical Research Letters*, 31(12). <https://doi.org/10.1029/2004gl020216>
- Fetterer, F., Knowles, K., Meier, W. N., Savoie, M., & Windnagel, A. K. (2017). *Sea ice index, version 3. [Years 1978-2019]*. NSIDC: National Snow and Ice Data Center. <https://doi.org/10.7265/N5K072F8>
- Freitas, F. S., Pika, P. A., Kasten, S., Jørgensen, B. B., Rassmann, J., Rabouille, C., et al. (2021). New insights into large-scale trends of apparent organic matter reactivity in marine sediments and patterns of benthic carbon transformation. *Biogeosciences*, 18(15), 4651–4679. <https://doi.org/10.5194/bg-18-4651-2021>
- Froelich, P. N., Klinkhammer, G., Bender, M. L., Luedtke, N., Heath, G. R., Cullen, D., et al. (1979). Early oxidation of organic matter in pelagic sediments of the eastern equatorial Atlantic: Suboxic diagenesis. *Geochimica et Cosmochimica Acta*, 43(7), 1075–1090. [https://doi.org/10.1016/0016-7037\(79\)90095-4](https://doi.org/10.1016/0016-7037(79)90095-4)
- Garibotti, I. A., Vernet, M., Smith, R. C., & Ferrario, M. E. (2005). Interannual variability in the distribution of the phytoplankton standing stock across the seasonal sea-ice zone west of the Antarctic Peninsula. *Journal of Plankton Research*, 27(8), 825–843. <https://doi.org/10.1093/plankt/fbi056>
- Goldberg, E. D. (1963). Geochronology with ²¹⁰Pb. Paper presented at the Symposium on radioactive dating 1962.
- Hatta, M., Measures, C. I., Selph, K. E., Zhou, M., & Hiscock, W. T. (2013). Iron fluxes from the shelf regions near the South Shetland islands in the Drake passage during the austral-winter 2006. *Deep Sea Research Part II: Topical Studies in Oceanography*, 90, 89–101. <https://doi.org/10.1016/j.dsr2.2012.11.003>
- Henkel, S., Kasten, S., Hartmann, J. F., Silva-Busso, A., & Staubwasser, M. (2018). Iron cycling and stable Fe isotope fractionation in Antarctic shelf sediments, King George Island. *Geochimica et Cosmochimica Acta*, 237, 320–338. <https://doi.org/10.1016/j.gca.2018.06.042>
- Herbert, L. C., Zhu, Q., Michaud, A. B., Laufer-Meiser, K., Jones, C. K., Riedinger, N., et al. (2021). Benthic iron flux influenced by climate-sensitive interplay between organic carbon availability and sedimentation rate in Arctic fjords. *Limnology and Oceanography*, 66(9), 3374–3392. <https://doi.org/10.1002/lno.11885>
- Holmkvist, L., Arning, E. T., Küster-Heins, K., Vandieken, V., Peckmann, J., Zabel, M., & Jørgensen, B. B. (2010). Phosphate geochemistry, mineralization processes, and Thioploca distribution in shelf sediments off central Chile. *Marine Geology*, 277(1–4), 61–72. <https://doi.org/10.1016/j.margeo.2010.08.011>
- Jahnke, R. A., & Jackson, G. A. (1992). The spatial distribution of sea floor oxygen consumption in the Atlantic and Pacific Oceans. In *Deep-sea food chains and the global carbon cycle* (pp. 295–307). Springer. https://doi.org/10.1007/978-94-011-2452-2_18
- Jørgensen, B. B., & Kasten, S. (2006). Sulfur cycling and methane oxidation. In H. D. Schulz, & M. Zabel (Eds.), *Marine geochemistry* (pp. 271–309). Springer Berlin Heidelberg. https://doi.org/10.1007/3-540-32144-6_8
- Jørgensen, B. B., Weber, A., & Zopf, J. (2001). Sulfate reduction and anaerobic methane oxidation in Black Sea sediments. *Deep-Sea Research I*, 48, 2097–2120. [https://doi.org/10.1016/S0967-0637\(01\)00007-3](https://doi.org/10.1016/S0967-0637(01)00007-3)
- Katsev, S., & Crowe, S. A. (2015). Organic carbon burial efficiencies in sediments: The power law of mineralization revisited. *Geology*, 43(7), 607–610. <https://doi.org/10.1130/g36626.1>
- Klunder, M., Laan, P., De Baar, H., Middag, R., Neven, I., & Van Ooijen, J. (2014). Dissolved Fe across the Weddell Sea and Drake passage: Impact of DFe on nutrient uptake. *Biogeosciences*, 11(3), 651–669. <https://doi.org/10.5194/bg-11-651-2014>
- Kraal, P., van Genuchten, C. M., Behrends, T., & Rose, A. L. (2019). Sorption of phosphate and silicate alters dissolution kinetics of poorly crystalline iron (oxyhydr) oxide. *Chemosphere*, 234, 690–701. <https://doi.org/10.1016/j.chemosphere.2019.06.071>
- Kraal, P., van Genuchten, C. M., Lenstra, W. K., & Behrends, T. (2020). Coprecipitation of phosphate and silicate affects environmental iron (oxyhydr) oxide transformations: A gel-based diffusive sampler approach. *Environmental Science & Technology*, 54(19), 12795–12802. <https://doi.org/10.1021/acs.est.0c02352>
- Küster-Heins, K., de Lange, G. J., & Zabel, M. (2010). Benthic phosphorus and iron budgets for three NW African slope sediments: A balance approach. *Biogeosciences*, 7(2), 469–480. <https://doi.org/10.5194/bg-7-469-2010>
- Küster-Heins, K., Steinmetz, E., De Lange, G. J., & Zabel, M. (2010). Phosphorus cycling in marine sediments from the continental margin off Namibia. *Marine Geology*, 274(1), 95–106. <https://doi.org/10.1016/j.margeo.2010.03.008>

- Lancelot, C., De Montety, A., Goosse, H., Becquevort, S., Schoemann, V., Pasquer, B., & Vancoppenolle, M. (2009). Spatial distribution of the iron supply to phytoplankton in the Southern Ocean: A model study. *Biogeosciences*, 6(12), 2861–2878. <https://doi.org/10.5194/bg-6-2861-2009>
- Laufer-Meisner, K., Michaud, A. B., Maisch, M., Byrne, J. M., Kappler, A., Patterson, M. O., et al. (2021). Potentially bioavailable iron produced through benthic cycling in glaciated Arctic fjords of Svalbard. *Nature Communications*, 12(1), 1349. <https://doi.org/10.1038/s41467-021-21558-w>
- Martin, J. H., Gordon, R. M., & Fitzwater, S. E. (1990). Iron in Antarctic waters. *Nature*, 345(6271), 156–158. <https://doi.org/10.1038/345156a0>
- März, C., Hoffmann, J., Bleil, U., de Lange, G. J., & Kasten, S. (2008). Diagenetic changes of magnetic and geochemical signals by anaerobic methane oxidation in sediments of the Zambesi deep-sea fan (SW Indian Ocean). *Marine Geology*, 255(3–4), 118–130. <https://doi.org/10.1016/j.margeo.2008.05.013>
- März, C., Riedinger, N., Sena, C., & Kasten, S. (2018). Phosphorus dynamics around the sulphate-methane transition in continental margin sediments: Authigenic apatite and Fe (II) phosphates. *Marine Geology*, 404, 84–96. <https://doi.org/10.1016/j.margeo.2018.07.010>
- Measures, C. I., Brown, M. T., Selph, K. E., Apprill, A., Zhou, M., Hatta, M., & Hiscock, W. T. (2013). The influence of shelf processes in delivering dissolved iron to the HNLC waters of the Drake Passage, Antarctica. *Deep Sea Research Part II: Topical Studies in Oceanography*, 90, 77–88. <https://doi.org/10.1016/j.dsr2.2012.11.004>
- Middelburg, J. J., Vlug, T., Jaco, F., & Van der Nat, W. (1993). Organic matter mineralization in marine systems. *Global and Planetary Change*, 8(1–2), 47–58. [https://doi.org/10.1016/0921-8181\(93\)90062-s](https://doi.org/10.1016/0921-8181(93)90062-s)
- Mitchell, B. G., & Holm-Hansen, O. (1991). Observations of modeling of the Antarctic phytoplankton crop in relation to mixing depth. *Deep-Sea Research, Part A: Oceanographic Research Papers*, 38(8–9), 981–1007. [https://doi.org/10.1016/0198-0149\(91\)90093-u](https://doi.org/10.1016/0198-0149(91)90093-u)
- Monien, P., Lettmann, K. A., Monien, D., Asendorf, S., Wöfl, A.-C., Lim, C. H., et al. (2014). Redox conditions and trace metal cycling in coastal sediments from the maritime Antarctic. *Geochimica et Cosmochimica Acta*, 141, 26–44. <https://doi.org/10.1016/j.gca.2014.06.003>
- Nickel, M., Vandieken, V., Brüchert, V., & Jørgensen, B. B. (2008). Microbial Mn(IV) and Fe(III) reduction in Northern Barents Sea sediments under different conditions of ice cover and organic carbon deposition. *Deep Sea Research Part II: Topical Studies in Oceanography*, 55(20), 2390–2398. <https://doi.org/10.1016/j.dsr2.2008.05.003>
- Nielsdóttir, M. C., Bibby, T. S., Moore, C. M., Hinz, D. J., Sanders, R., Whitehouse, M., et al. (2012). Seasonal and spatial dynamics of iron availability in the Scotia Sea. *Marine Chemistry*, 130, 62–72. <https://doi.org/10.1016/j.marchem.2011.12.004>
- Niewöhner, C., Hensen, C., Kasten, S., Zabel, M., & Schulz, H. (1998). Deep sulfate reduction completely mediated by anaerobic methane oxidation in sediments of the upwelling area off Namibia. *Geochimica et Cosmochimica Acta*, 62(3), 455–464. [https://doi.org/10.1016/S0016-7037\(98\)00055-6](https://doi.org/10.1016/S0016-7037(98)00055-6)
- Noffke, A., Hensen, C., Sommer, S., Scholz, F., Bohlen, L., Mosch, T., et al. (2012). Benthic iron and phosphorus fluxes across the Peruvian oxygen minimum zone. *Limnology and Oceanography*, 57(3), 851–867. <https://doi.org/10.4319/lom.2012.57.3.0851>
- O’Loughlin, E. J., Boyanov, M. I., Gorski, C. A., Scherer, M. M., & Kemmer, K. M. (2021). Effects of Fe(III) oxide Mineralogy and phosphate on Fe(II) secondary mineral formation during microbial iron reduction. *Minerals*, 11(2), 149. <https://doi.org/10.3390/min111020149>
- Oni, O., Miyatake, T., Kasten, S., Richter-Heitmann, T., Fischer, D., Wagenknecht, L., et al. (2015). Distinct microbial populations are tightly linked to the profile of dissolved iron in the methanic sediments of the Helgoland mud area, North Sea. *Frontiers in Microbiology*, 6(365). <https://doi.org/10.3389/fmicb.2015.00365>
- Paytan, A., & McLaughlin, K. (2007). The oceanic phosphorus cycle. *Chemical Reviews*, 107(2), 563–576. <https://doi.org/10.1021/cr0503613>
- Poulton, S. W., Krom, M. D., & Raiswell, R. (2004). A revised scheme for the reactivity of iron (oxyhydr)oxide minerals towards dissolved sulfide. *Geochimica et Cosmochimica Acta*, 68(18), 3703–3715. <https://doi.org/10.1016/j.gca.2004.03.012>
- Raiswell, R., Benning, L. G., Tranter, M., & Tulacz, S. (2008). Bioavailable iron in the Southern Ocean: The significance of the iceberg conveyor belt. *Geochemical Transactions*, 9(1), 7. <https://doi.org/10.1186/1467-4866-9-7>
- Raiswell, R., Hawkins, J. R., Benning, L. G., Baker, A. R., Death, R., Albani, S., et al. (2016). Potentially bioavailable iron delivery by iceberg-hosted sediments and atmospheric dust to the polar oceans. *Biogeosciences*, 13(13), 3887–3900. <https://doi.org/10.5194/bg-13-3887-2016>
- Sachs, O., Sauter, E. J., Schlüter, M., van der Loeff, M. M. R., Jerosch, K., & Holby, O. (2009). Benthic organic carbon flux and oxygen penetration reflect different plankton provinces in the Southern Ocean. *Deep-Sea Research Part I Oceanographic Research Papers*, 56(8), 1319–1335. <https://doi.org/10.1016/j.dsr.2009.02.003>
- Sakshaug, E., Slagstad, D., & Holm-Hansen, O. (1991). Factors controlling the development of phytoplankton blooms in the Antarctic ocean—A mathematical model. *Marine Chemistry*, 35(1–4), 259–271. [https://doi.org/10.1016/s0304-4203\(99\)90021-4](https://doi.org/10.1016/s0304-4203(99)90021-4)
- Savidge, G., Harbour, D., Gilpin, L., & Boyd, P. (1995). Phytoplankton distributions and production in the Bellingshausen sea, austral spring 1992. *Deep Sea Research Part II: Topical Studies in Oceanography*, 42(4–5), 1201–1224. [https://doi.org/10.1016/0967-0645\(95\)00062-u](https://doi.org/10.1016/0967-0645(95)00062-u)
- Schloss, I. R., Ferreyra, G. A., & Ruiz-Pino, D. (2002). Phytoplankton biomass in Antarctic shelf zones: A conceptual model based on Potter Cove, King George island. *Journal of Marine Systems*, 36(3–4), 129–143. [https://doi.org/10.1016/s0924-7963\(02\)00183-5](https://doi.org/10.1016/s0924-7963(02)00183-5)
- Schnakenberg, A., Aromokeye, D. A., Kulkarni, A., Maier, L., Wunder, L. C., Richter-Heitmann, T., et al. (2021). Electron acceptor availability shapes anaerobically methane oxidizing archaea (ANME) communities in South Georgia sediments. *Frontiers in Microbiology*, 12. <https://doi.org/10.3389/fmicb.2021.617280>
- Schulz, H. D., Dahmke, A., Schinzel, U., Wallmann, K., & Zabel, M. (1994). Early diagenetic processes, fluxes, and reaction rates in sediments of the South Atlantic. *Geochimica et Cosmochimica Acta*, 58(9), 2041–2060. [https://doi.org/10.1016/0016-7037\(94\)90284-4](https://doi.org/10.1016/0016-7037(94)90284-4)
- Sedwick, P. N., DiTullio, G. R., & Mackey, D. J. (2000). Iron and manganese in the Ross Sea, Antarctica: Seasonal iron limitation in Antarctic shelf waters. *Journal of Geophysical Research*, 105(C5), 11321–11336. <https://doi.org/10.1029/2000jc000256>
- Seeberg-Elverfeldt, J., Schlüter, M., Feseker, T., & Kölling, M. (2005). Rhizon sampling of porewaters near the sediment-water interface of aquatic systems. *Limnology and Oceanography: Methods*, 3(8), 361–371. <https://doi.org/10.4319/lom.2005.3.361>
- Seiter, K., Hensen, C., & Zabel, M. (2005). Benthic carbon mineralization on a global scale. *Global Biogeochemical Cycles*, 19(1). <https://doi.org/10.1029/2004gb002225>
- Slomp, C., Van der Gaast, S., & Van Raaphorst, W. (1996). Phosphorus binding by poorly crystalline iron oxides in North Sea sediments. *Marine Chemistry*, 52(1), 55–73. [https://doi.org/10.1016/0304-4203\(95\)00078-x](https://doi.org/10.1016/0304-4203(95)00078-x)
- Smith, C. R., Mincks, S., & De Master, D. J. (2006). A synthesis of benthic-pelagic coupling on the Antarctic shelf: Food banks, ecosystem inertia and global climate change. *Deep Sea Research Part II: Topical Studies in Oceanography*, 53(8–10), 875–894. <https://doi.org/10.1016/j.dsr2.2006.02.001>
- Spren, G., Kaleschke, L., & Heygster, G. (2008). Sea ice remote sensing using AMSR-E 89 GHz channels. *Journal of Geophysical Research*, 113, C02S03. <https://doi.org/10.1029/2005JC003384>
- Tessin, A., März, C., Kędra, M., Matthiessen, J., Morata, N., Nairn, M., et al. (2020). Benthic phosphorus cycling within the Eurasian marginal sea ice zone. *Philosophical Transactions of the Royal Society A*, 378(2181), 20190358. <https://doi.org/10.1098/rsta.2019.0358>

- Vaughan, D. G., Marshall, G. J., Connolley, W. M., Parkinson, C., Mulvaney, R., Hodgson, D. A., et al. (2003). Recent rapid regional climate warming on the Antarctic Peninsula. *Climatic Change*, *60*(3), 243–274. <https://doi.org/10.1023/a:1026021217991>
- Venables, H. J., & Meredith, M. P. (2009). Theory and observations of Ekman flux in the chlorophyll distribution downstream of South Georgia. *Geophysical Research Letters*, *36*(23), L23610. <https://doi.org/10.1029/2009gl041371>
- Vernet, M., Martinson, D., Iannuzzi, R., Stammerjohn, S., Kozłowski, W., Sines, K., et al. (2008). Primary production within the sea-ice zone West of the Antarctic Peninsula: I—sea Ice, summer mixed layer, and irradiance. *Deep Sea Research Part II: Topical Studies in Oceanography*, *55*(18), 2068–2085. <https://doi.org/10.1016/j.dsr2.2008.05.021>
- Voegelin, A., Senn, A.-C., Kaegi, R., Hug, S. J., & Mangold, S. (2013). Dynamic Fe-precipitate formation induced by Fe (II) oxidation in aerated phosphate-containing water. *Geochimica et Cosmochimica Acta*, *117*, 216–231. <https://doi.org/10.1016/j.gca.2013.04.022>
- Volz, J. B., Liu, B., Köster, M., Henkel, S., Koschinsky, A., & Kasten, S. (2020). Post-depositional manganese mobilization during the last glacial period in sediments of the Eastern Clarion-Clipperton Zone, Pacific Ocean. *Earth and Planetary Science Letters*, *532*, 116012. <https://doi.org/10.1016/j.epsl.2019.116012>
- Wadham, J. L., De'Ath, R., Monteiro, F., Tranter, M., Ridgwell, A., Raiswell, R., & Tulaczyk, S. (2013). The potential role of the Antarctic ice sheet in global biogeochemical cycles. *Earth and Environmental Science Transactions of the Royal Society of Edinburgh*, *104*(1), 55–67. <https://doi.org/10.1017/S1755691013000108>
- Wehrmann, L. M., Formolo, M. J., Owens, J. D., Raiswell, R., Ferdelman, T. G., Riedinger, N., & Lyons, T. W. (2014). Iron and manganese speciation and cycling in glacially influenced high-latitude fjord sediments (West Spitsbergen, Svalbard): Evidence for a benthic recycling-transport mechanism. *Geochimica et Cosmochimica Acta*, *141*, 628–655. <https://doi.org/10.1016/j.gca.2014.06.007>
- Wehrmann, L. M., Riedinger, N., Brunner, B., Kamyshny, A., Hubert, C. R. J., Herbert, L. C., et al. (2017). Iron-controlled oxidative sulfur cycling recorded in the distribution and isotopic composition of sulfur species in glacially influenced fjord sediments of west Svalbard. *Chemical Geology*, *466*, 678–695. <https://doi.org/10.1016/j.chemgeo.2017.06.013>
- Wenzhöfer, F., & Glud, R. N. (2002). Benthic carbon mineralization in the Atlantic: A synthesis based on in situ data from the last decade. *Deep Sea Research Part I: Oceanographic Research Papers*, *49*(7), 1255–1279. [https://doi.org/10.1016/S0967-0637\(02\)00025-0](https://doi.org/10.1016/S0967-0637(02)00025-0)
- Weston, N. B., Porubsky, W. P., Samarkin, V. A., Erickson, M., Macavoy, S. E., & Joye, S. B. (2006). Porewater stoichiometry of terminal metabolic products, sulfate, and dissolved organic carbon and nitrogen in estuarine intertidal creek-bank sediments. *Biogeochemistry*, *77*(3), 375–408. <https://doi.org/10.1007/s10533-005-1640-1>
- Wunder, L. C., Aromokeye, D. A., Yin, X., Richter-Heitmann, T., Willis-Poratti, G., Schnakenberg, A., et al. (2021). Iron and sulfate reduction structure microbial communities in (sub-)Antarctic sediments. *The ISME Journal*, *15*(12), 3587–3604. <https://doi.org/10.1038/s41396-021-01014-9>
- Zonneveld, K. A., Versteegh, G. J., Kasten, S., Eglinton, T. I., Emeis, K.-C., Huguët, C., et al. (2010). Selective preservation of organic matter in marine environments; processes and impact on the sedimentary record. *Biogeosciences*, *7*(2), 483–511. <https://doi.org/10.5194/bg-7-483-2010>